7-1-2020

Multi-omics: Differential expression of IFN-γ results in distinctive mechanistic features linking chronic inflammation, gut dysbiosis, and autoimmune diseases

Heekyong R. Bae
National Cancer Institute at Frederick, baehee@gmail.com

Patrick S.C. Leung
University of California, Davis, psleung@ucdavis.edu

Deborah L. Hodge
National Cancer Institute at Frederick, hodged@mail.nih.gov

John M. Fenimore
National Cancer Institute at Frederick, john.fenimore@nih.gov

Seon Min Jeon
Kyungpook National University, smjeon111@gmail.com

See next page for additional authors

Journal of Autoimmunity 111 (2020) 102436

Contents lists available at ScienceDirect

Journal of Autoimmunity

journal homepage: www.elsevier.com/locate/jautimm

Multi-omics: Differential expression of IFN-γ results in distinctive mechanistic features linking chronic inflammation, gut dysbiosis, and autoimmune diseases

Heekyong R. Bae[a], Patrick S.C. Leung[b], Deborah L. Hodge[a], John M. Fenimore[a], Seon-Min Jeon[c], Vishal Thovarai[a], Amiran Dzutsev[a], Andrew A. Welcher[d], Michael Boedigheimer[d], Michael A. Damore[d], Myung-Sook Choi[c], Richard A. Fravell[e], Giorgio Trinchieri[a], M. Eric Gershwin[b,**], Howard A. Young[a,*]

[a] Laboratory of Experimental Immunology, Cancer and Inflammation Program, Center for Cancer Research, National Cancer Institute-Frederick, Frederick, MD, USA
[b] Division of Rheumatology, Allergy and Clinical Immunology, University of California at Davis, Davis, CA, USA
[c] Center for Food and Nutritional Genomics Research, Department of Food Science and Nutrition, Kyungpook National University, Daegu, Republic of Korea
[d] Amgen Inc., Thousand Oaks, CA, USA
[e] Department of Immunology, Yale School of Medicine, New Haven, CT, USA

ARTICLE INFO

Keywords:
Multi-omics
Interferons
Chronic inflammation
Gut dysbiosis
Nuclear receptors
Autophagy
Sex-difference
Autoimmune diseases

ABSTRACT

Low grade, chronic inflammation is a critical risk factor for immunologic dysfunction including autoimmune diseases. However, the multiplicity of complex mechanisms and lack of relevant murine models limit our understanding of the precise role of chronic inflammation. To address these hurdles, we took advantage of multi-omics data and a unique murine model with a low but chronic expression of IFN-γ, generated by replacement of the AU-rich element (ARE) in the 3' UTR region of IFN-γ mRNA with random nucleotides. Herein, we demonstrate that low but differential expression of IFN-γ in mice by homozygous or heterozygous ARE replacement triggers distinctive gut microbial alterations, of which alteration is female-biased with autoimmune-associated microbiota. Metabolomics data indicates that gut microbiota-dependent metabolites have more robust sex-differences than microbiome profiling, particularly those involved in fatty acid oxidation and nuclear receptor signaling. More importantly, homozygous ARE-Del mice have dramatic changes in tryptophan metabolism, bile acid and long-chain lipid metabolism, which interact with gut microbiota and nuclear receptor signaling similarly with sex-dependent metabolites. Consistent with these findings, nuclear receptor signaling, encompassing molecules such as PPARs, FXR, and LXRs, was detectable as a top canonical pathway in comparison of blood and tissue-specific gene expression between female homozygous vs heterozygous ARE-Del mice. Further analysis implies that dysregulated autophagy in macrophages is critical for breaking self-tolerance and gut homeostasis, while pathways interact with nuclear receptor signaling to regulate inflammatory responses. Overall, pathway-based integration of multi-omics data provides systemic and cellular insights about how chronic inflammation driven by IFN-γ results in the development of autoimmune diseases with specific etiopathological features.

1. Introduction

Chronic inflammation lasts for several months to years and is associated with the most prevalent worldwide diseases, including autoimmune diseases [1]. Due to increases in obesity, population aging and environmental toxins as high-risk factors for chronic inflammation, more attention has been focused on understanding the etiological mechanisms that trigger chronic inflammation as well as defining its role

* Corresponding author. Cancer and Inflammation Program, Center for Cancer Research, National Cancer Institute-Frederick, and SAIC Frederick, Frederick, MD, 21702, USA.
** Corresponding author. Division of Rheumatology, Allergy and Clinical Immunology, University of California Davis School of Medicine, Davis, CA, 95616, USA.
E-mail addresses: baehee@gmail.com (H.R. Bae), psleung@ucdavis.edu (P.S.C. Leung), hodged@mail.nih.gov (D.L. Hodge), john.fenimore@nih.gov (J.M. Fenimore), smjeon111@gmail.com (S.-M. Jeon), vishal.thovarai@nih.gov (V. Thovarai), amiran.dzutsev@nih.gov (A. Dzutsev), andywelcher@yahoo.com (A.A. Welcher), mboedigh@outlook.com (M. Boedigheimer), mdamore@me.com (M.A. Damore), mschoi@knu.ac.kr (M.-S. Choi), richard.flavell@yale.edu (R.A. Fravell), trinchig@niaid.nih.gov (G. Trinchieri), megershwin@ucdavis.edu (M.E. Gershwin), younghow@mail.nih.gov (H.A. Young).

https://doi.org/10.1016/j.jaut.2020.102436
Received 25 November 2019; Received in revised form 26 February 2020; Accepted 5 March 2020
Available online 24 March 2020
0896-8411/ Published by Elsevier Ltd.

in disease. However, understanding the links between etiological and pathological features are poorly defined due to the complexity of the biological processes. Chronic inflammation and autoimmune diseases link together bi-directionally [2]; chronic inflammatory autoimmune disorders result in the production of cytokines and chemokines, which further lead to additional chronic inflammation-mediated disorders. Furthermore, prolonged inflammation, *e.g.* as a result of failing to clear pathogens, may trigger the development of autoimmune diseases [3]. One example of the consequences of cytokine dysregulation is the constant expression of interferons. Interferons are produced by immune cells to defend against infection and can act as antimicrobial and antiviral agents [4].

Chronic expression of interferons is seen in various autoimmune diseases including SLE, RA, and Sjogren's Syndrome [5,6], but the pathological mechanisms controlling interferon expression in autoimmune diseases is still not well understood. We recently engineered a murine model of chronic inflammation as a result of a low, persistent expression of interferon-gamma (IFN-γ) that mimics chronic inflammatory conditions in humans, through substitution of the AU-rich element (ARE) in the IFN-γ 3′ untranslated region (coined ARE-Del) with random nucleotides which results in low but chronic expression of IFN-γ [7]. We observed that the ARE-Del mice have autoimmune manifestations with striking clinical, immunological and histopathological characteristics of human primary biliary cirrhosis (PBC) with a female prevalence [8,9]. As major autoimmune diseases including SLE, RA, Sjogren's syndrome, and PBC have a high incidence in women [10], the mechanistic understanding of female-biased inflammatory responses is pivotal for the treatment of autoimmune diseases. Therefore, this model can be utilized for developing a mechanistic understanding of how chronic inflammation leads to autoimmune diseases.

Pathway-based analysis, known as a functional enrichment analysis focusing on biological functions, is a valuable tool to integrate multi-omics studies [11,12]. Particularly, immune responses are rapidly processed by post-transcriptional or post-translational modification [13,14], thus pathway analysis rather than individual gene signatures provide more adequate information for predicting immune responses. For example, even when individual gene expression levels (*e.g.* cytokines and surface markers) are not observed to be changed, their activation can be inferred by down-stream or correlated pathways. Here we present how we applied this tool to integrate different types of data sets and characterize target pathways and molecules in the immune system of mice.

Homozygous or heterozygous alleles at the IFN-γ locus result in differing levels of circulating IFN-γ [7]. The average serum level of IFN-γ in homozygous ARE-Del mice was measured to be ~30 pg/ml, compared to negligible levels of control mice, while heterozygous ARE-Del mice have generally less than ~15 pg/ml. Further, we characterized that the serum level of IFN-γ was more strongly expressed in female than male ARE-Del mice [8]. Phenotypically, both genotypes share similarities with respect to human PBC, such as portal lymphocytic infiltration and anti-mitochondrial antibody (AMA) production. Whereas, there are distinctive pathological and serological features, including loss of marginal zone B cells (MZB), increases of germinal center (GC) B cells and antinuclear antibody (ANA) production, specifically observed in homozygous ARE-Del mice. Based on our previous report that depletion of macrophages by clodronate liposomes (CLL) in heterozygous ARE-Del mice significantly increases the pathological phenotypes observed in homozygous ARE-Del mice, herein we focused on macrophage function and the mechanistic differences between heterozygous vs homozygous ARE-Del mice.

2. Materials and methods

2.1. Animals

ARE-Del mice were generated and maintained as previously reported [7,8]. Animal care was provided in accordance with the "Guide for Care and Use of Laboratory Animals" (National Research Council; 2011; National Academy Press: Washington, D.C.). The experimental protocols were approved by National Cancer Institute at Frederick and the University of California at Davis Animal Care and Use Committees. All experiments were performed in group sizes of 4–6, and the numbers in each experiment are noted in the figure legends.

2.2. Cecum microbiome analysis

The cecum microbiome composition of homozygous and heterozygous ARE-Del mice and control littermates at 4, 8 and 20 weeks of age were examined. Briefly, a harvested cecum section was rapidly frozen in dry ice and stored in −80 °C. Immediately after thawing, DNA was isolated using a Powersoil DNA isolation kit (MO Bio, CA), quantified and stored at −20 °C. The V4 region of the 16S rDNA gene (515F-806R) was sequenced; generating partially overlapping, paired-end reads on the Illumina MiSeq platform. The demultiplexed paired-end fastq files were pre-processed and analyzed using QIIME2 [15]. The DADA2 algorithm [16] implemented in QIIME2, was used for error modeling and filtering the raw fastq files. After denoising and chimera removal; a total of 1,656,000 sequences were retained for 51 samples. The taxonomic classification was performed using the QIIME2 feature-classifier plugin trained on the Silva 132 database [17]. The Alpha and Beta-diversity analyses were performed using the diversity plugin at a sampling depth of 24,000 reads per sample. Alpha diversity was calculated by Shannon's diversity index and observed operational taxonomic units (OTUs). Principal coordinate analysis (PCoA) was performed to calculate Beta diversity using Bray-Curtis distances, and pairwise Permutational Multivariate Analysis of Variance (PERMANOVA) was used to analyze statistical differences in beta diversity with QIIME2.

2.3. Blood and tissue-specific gene expression analysis

For global gene expression analysis, spleen, thymus, kidney, and blood were harvested from 3, 6 and 12-week old homozygous and heterozygous ARE-Del mice compared to control littermates (Each group has at least three replicates and total sample numbers are 218). To extract RNA from the spleen, thymus, and kidney, 1 ml of Trizol per 50–100 mg of tissue was homogenized with a TissueRuptor (Qiagen). RNA samples were prepared by the conventional phenol-chloroform RNA extraction. To prepare RNA from peripheral blood mononuclear cells (PBMCs), approximately 1 ml of blood per mouse were collected by cardiac puncture under anesthesia and diluted 1:1 with PBS. PBMCs were then obtained by gradient centrifugation using sterile-filtered histopaque 1077 (Sigma), washed and resuspended in sterile PBS. RNA was then purified as above using 10X volume of Trizol to cell ratio. RNA was quantified by Nanodrop (Thermo Scientific) and assessed by Bioanalyzer 2100 (Agilent Technologies). Transcriptional differences between homozygous and heterozygous ARE-Del mice were compared with control littermates using microarray analysis. Briefly, Cy3-labeled complementary DNA was generated using the Low Input Quick Amp Labeling Kit, one-color (Agilent Technologies) and hybridized to a custom 180k Agilent array with the content of the Human Gene Expression 44K replicated four times (AMADID#026822; Agilent Technologies). Analyses were conducted with log2-transformed intensities that had been normalized at the array level to have a comparable intensity spectrum. Further statistical analysis of homozygous ARE-Del mice, heterozygotes with control littermates in each tissue and age was performed by Partek Genomics Suite 6.6 (v6.14.006).

2.4. Plasma metabolome analysis

Plasma was collected from 16 weeks old male and female homozygous ARE-Del mice (each n = 6, total n = 12) and control littermates

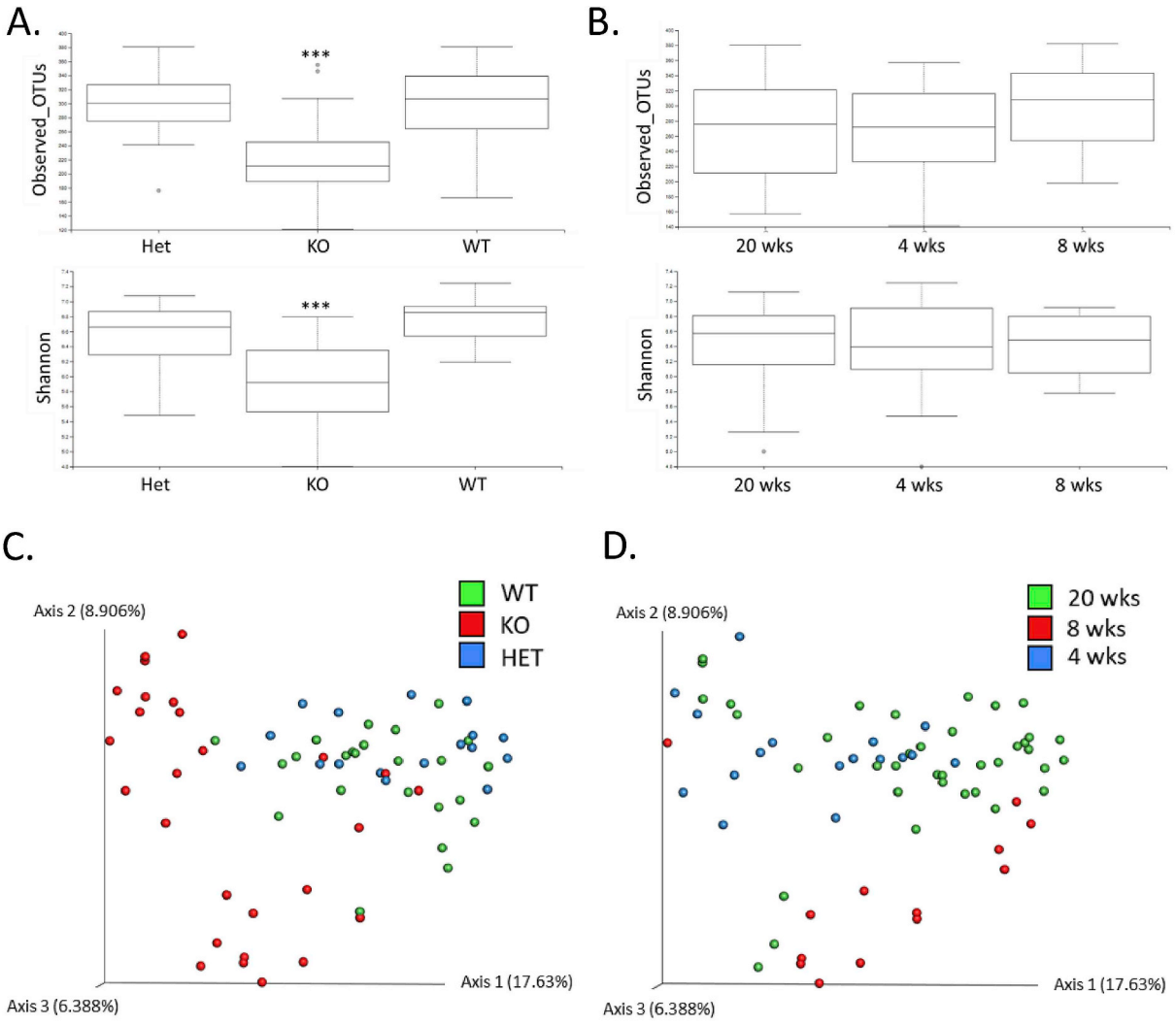

(caption on next page)

Fig. 1. Comparison of cecal microbial profiles from homozygous and heterozygous ARE-Del mice. (A) Boxplots of observed OTUs richness and Shannon diversity indexes comparing cecum samples from homozygous (n = 27) and heterozygous (n = 17) ARE-Del mice with control littermates (n = 24) at 20 weeks old. Kruskal-Wallis test was performed to analyze the significance (***$p < 0.0001$). (B) Boxplots of observed OTUs richness and Shannon diversity indexes comparing different ages of 4 weeks (n = 17), 8 weeks (n = 13) and 20 weeks (n = 39). (C) A PCoA plot of cecum samples from homozygous (KO) and heterozygous (Het) mice with control littermates (WT). (D) A PCoA plot of cecum samples collected at 4, 8 and 20 weeks of age. (C–D) Pairwise Permanova was also used to estimate beta group significance. (E) Heat map of relative expression values of normalized counts for the significant changes ($p < 0.05$) at the genus level in female and male homozygous and heterozygous ARE-Del mice compared to control littermates.

(each n = 6, total n = 12), and stored at −80 °C. Metabolome analysis was performed at Metabolon, Inc (Durham, NC), as previously described [18]. Briefly, sample preparation was conducted using a proprietary series of organic and aqueous extractions to remove the protein fraction while allowing maximum recovery of small molecules. Each sample was then frozen and dried under vacuum. Samples were then prepared for the appropriate instrument, either LC/MS or GC/MS. The LC/MS portion of the platform was based on a Waters Acquity UPLC and a Thermo-Finnigan LTQ-FT mass spectrometer, which consists of an electrospray ionization (ESI) source and a linear ion-trap (LIT) front end and a Fourier transform ion cyclotron resonance (FT-ICR) mass spectrometer backend. Fragmentation spectra (MS/MS) was employed, such as in the case of lower level signals. One aliquot was analyzed using acidic positive ion optimized conditions and the other using basic negative ion optimized conditions in two independent injections using separate dedicated columns. Extracts reconstituted in acidic conditions were gradient eluted using water and methanol both containing 0.1% formic acid, while the basic extracts, which also used water/methanol, contain 6.5 mM ammonium bicarbonate. The samples destined for GC/MS analysis were re-dried under vacuum desiccation for a minimum of 24 h prior to being derivatized under dried nitrogen using bistrimethylsilyl-triflouroacetamide (BSTFA). The GC column was 5% phenyl and the temperature ramp was from 40° to 300 °C in a 16 min period. Samples were analyzed on a Thermo-Finnigan Trace DSQ fast-scanning single-quadrupole mass spectrometer using electron impact ionization. For data analysis including the data extraction, quality control, compound identification, curation, and normalization, we used instrument vendor-supplied or in-house software.

2.5. MicroRNA expression data analysis

Total RNA enriched with miRNA from the thymus was extracted using miRNeasy Mini Kit (Qiagen, Hilden, Germany) following the manufacturer's protocol. 100 ng of RNA was used as input for the NanoString platform (Nanostring, Seattle, WA). DNA sequences called miRtags were ligated to the mature miRNAs and unligated miRtags were removed by enzymatic purification. The miRtagged mature miRNA was hybridized with a nCounter miRNA Expression Assay CodeSet overnight at 65 °C. The unhybridized CodeSet was eliminated by automated purification on a nCounter Prep station, and the hybridized CodeSet was analyzed and raw data were collected through a nCounter Digital Analyzer. Data normalization was performed on nSolver and differentially expressed miRNAs were analyzed by Partek Genomics Suite.

2.6. Detection of autophagosome formation

Female homozygous ARE-Del and control littermates were used to isolate bone marrow cells which were flushed from the femur and tibia. To differentiate bone marrow-derived macrophages, cells were cultured with 25 ng/ml murine GM-CSF (Miltenyi Biotech) for 7–10 days. Attached cells were further isolated to measure autophagosomes using Cyto-ID detection kit (Enzo Life Sciences, Farmingdale, NY), which has a cationic amphiphilic tracer dye to stain selectively autophagic vacuoles. Briefly, cells were treated with 3 μM rapamycin and incubated at 37 °C for 2 h. Cells were collected after PBS washing and incubated for 30 min with the detection reagent containing dyes for autophagic vacuoles and nuclear (Hoechst 33,342). After PBS washes, the cells were fixed with 4% paraformaldehyde for 20 min in the dark and immediately pictured under a Leica TCS SP8 laser scanning confocal microscope with a 63X objective.

3. Results

3.1. Cecal microbiota are distinctively altered by low, but differential levels of IFNγ

To investigate whether low but chronic expression of IFN-γ affects the gut microbiome, we performed 16S rRNA analysis on cecum microbial populations between sample groups of homozygous, heterozygous ARE-Del mice, and control littermates at 4, 8, and 20 weeks of age. Cecal microbial profiling demonstrated that there are distinct differences in the diversity and richness in cecum bacterial populations between these mice. The observed OTUs and Shannon index indicate that there was a significant alteration in homozygotes when compared with heterozygotes and control mice (Fig. 1A), while there were no significant changes of these indexes between age groups (Fig. 1B). Consistently, the microbial beta diversity represented by PCoA plots with Pairwise Permanova, demonstrated that homozygous ARE-Del mice cluster significantly differently ($p < 0.05$) from heterozygotes and the control group on axis 1 (17.6%) (Fig. 1C). Although there was a slight diversity in the PCoA plot demonstrating different age groups (Fig. 1D), all pairwise adjusted p values between age groups were < 0.05, indicating age-related changes in the gut microbiome. Significant changes ($p < 0.05$) in microbiota amongst ARE-Del homo-, heterozygotes, and wild type at the genus level are represented as heat maps, which were separated by log2 fold changes (0–5 and 5 to 10) (Fig. 1E). The pattern of changes in homozygous ARE-Del was generally reduced when compared to heterozygous ARE-Del and control littermates, indicating the lower microbial diversity in homozygous ARE-Del mice as one of makers for gut dysbiosis. Notably, homozygous mice specifically increased genera, including *Desulfovibrio*, *Roseburia*, and *Alistipes*, that have been associated with various autoimmune diseases.

3.2. Sex-difference in gut dysbiosis with autoimmune disease-associated gut microbiota

Although sex-specific microbial profiles have been reported in human and various mouse strains, it is not well understood whether sex-specific microbial profiles are associated with the development of autoimmune diseases. Thus, we further analyzed microbial changes at the genus level to examine the difference between male and female homozygous ARE-Del mice (Fig. 2). Although the observed OTUs and Shannon index (Fig. 2A) and beta diversity (Fig. 2B) were not significantly different between male and female homozygous ARE-Del mice, there were statistically significant ($p < 0.05$) diversities when

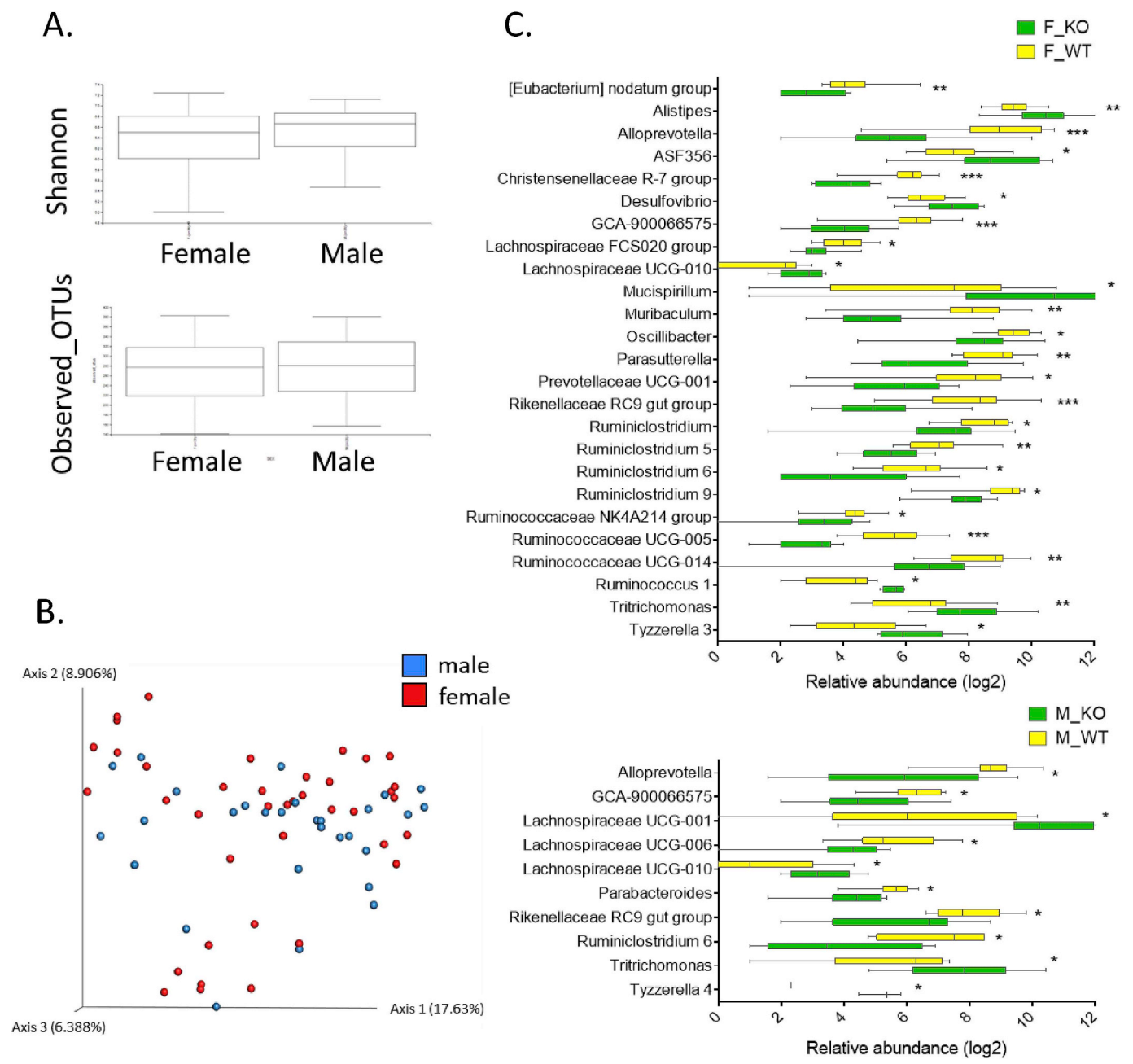

Fig. 2. Sex-specific cecal microbial profiles in homozygous ARE-Del mice. (A) Boxplots of observed OTUs richness and Shannon diversity indexes and (B) A PCoA plot comparing cecum samples from female (n = 40) and male (n = 29) mice (all genotypes combined). (C) Bar graphs of sex-specific intestinal bacteria at the genus level. The upper graph presents significantly changed bacteria between female homozygous ARE-Del mice (F_KO) and control female littermates (F_WT). The lower graph presents data comparing male homozygous ARE-Del mice (M_KO) and control male littermates (M_WT). The abundance of genera was converted into log fold ratio (Log2) and each bar shows mean with SEM. Statistical analysis is performed by multiple *t*-test (no multiple comparisons), *P < 0.05, **P < 0.001, ***P < 0.001.

male and female mice were separately analyzed at the genus level (Fig. 2C). Female homozygous ARE-Del mice had significantly increased genera of *Alistipes*, *ASF356*, *Desulfovibrio*, *Lachnospiraceae UCG-010*, *Mucispirillum, Ruminococcus 1, Trichomonas, and Tyzzerella 3*. However, *Alloprevotella, Christensenellaceae R-7 group*, *GCA-900066575*, *Lachnospiraceae FCS020 group*, *Muribaculum*, *Oscillibacter, Parasutterella, Prevotellaceae UCG-001, Rikenellaceae RC9, Ruminiclostridium, Ruminislostridium 5, Ruminislostridium 6, Ruminislostridium 9, Ruminococcaceae UCG-005*, and *Ruminococcaceae UCG-014* were less abundant in female homozygous ARE-Del mice than control littermates. In male homozygous ARE-Del mice, *Lachnospiraceae UCG-001, Lachnospiraceae UCG-010, Tritrichomonas, and Tyzzerella 4* significantly increased, while the abundance of *Alloprevotella, GCA-900066575, Lachnospiraceae UCG-006, Parabacteroides, Rikenellaceae RC9 gut group*, and *Ruminislostridium 6* were suppressed.

3.3. Robust sex differences in energy and lipid metabolism in homozygous ARE-Del mice, associated with the gut microbiome and nuclear receptor signaling

As cecal microbiome was strongly changed as early as 4 weeks old in homozygous ARE-Del mice, we thus further analyzed metabolomics profiles in the plasma at 4 weeks of age between male and female homozygous ARE-Del mice compared to control littermates. This

Table 1

Representative average fold changes of serum metabolites in male and female homozygous ARE-Del mice compared to control wild-type mice. Significant fold changes are marked by red and green colors ($p < 0.05$). All KO; both male and female homozygous ARE-Del mice (n = 12) vs control littermates (n = 12), KO F; female homozygous ARE-Del mice (n = 6) vs control littermates (n = 6), KO M; male homozygous ARE-Del mice (n = 6) vs control littermates (n = 6).

SUPER PATHWAY	SUB PATHWAY	BIOCHEMICAL	ALL KO /	KO F /	KO M /
Amino acid	Alanine and aspartate metabolism	3-ureidopropionate	1.12	1.11	1.13
	Butanoate metabolism	2-aminobutyrate	0.89	0.77	1.08
	Cysteine, methionine, SAM, taurine metabolism	2-hydroxybutyrate (AHB)	0.85	0.77	0.99
		methionine	1.48	1.85	1.20
		N-acetylmethionine	1.41	1.64	1.20
	Glutamate metabolism	glutamine	0.85	0.88	0.81
		N-acetylglutamine	0.77	0.98	0.64
	Glycine, serine and threonine metabolism	beta-hydroxypyruvate	0.86	1.22	0.61
		betaine	0.95	0.88	1.03
		glycine	1.10	1.09	1.11
		N-acetylglycine	0.68	0.47	0.95
	Guanidino and acetamido metabolism	4-guanidinobutanoate	1.46	1.67	1.28
	Histidine metabolism	histidine	0.89	0.97	0.82
		urocanate	0.69	0.54	1.01
	Lysine metabolism	lysine	0.76	0.73	0.79
		N6-acetyllysine	1.23	1.30	1.16
		pipecolate	0.88	1.06	0.76
	Phenylalanine & tyrosine metabolism	3-(4-hydroxyphenyl)lactate	1.37	1.44	1.27
		4-hydroxyphenylpyruvate	1.49	1.75	1.21
		N-acetylphenylalanine	1.32	1.55	1.06
		N-acetyltyrosine	1.38	1.84	0.99
		p-cresol sulfate	0.25	0.41	0.08
		phenylalanine	1.07	1.20	0.95
		phenyllactate (PLA)	1.71	1.83	1.60
		tyrosine	1.20	1.39	1.03
	Polyamine metabolism	5-methylthioadenosine (MTA)	1.31	1.33	1.29
	Tryptophan metabolism	3-indoxyl sulfate	1.07	1.09	1.04
		indolelactate	1.39	1.41	1.36
		kynurenine	3.31	2.55	5.07
		N-acetyltryptophan	0.78	0.91	0.62
		serotonin (5HT)	0.55	0.44	0.71
		tryptophan	0.78	0.80	0.75
	Urea cycle; arginine-, proline-, metabolism	citrulline	1.29	1.35	1.23
		dimethylglycine	1.27	1.22	1.35
		homocitrulline	1.52	1.22	1.88
		homostachydrine*	0.81	0.79	0.82
		proline	1.50	1.73	1.30
		urea	1.29	1.54	1.08
	Valine, leucine and isoleucine metabolism	2-hydroxy-3-methylvalerate	0.96	1.30	0.83
		2-methylbutyroylcarnitine	1.34	1.23	1.47
		3-methyl-2-oxobutyrate	0.74	0.69	0.80
		3-methyl-2-oxovalerate	0.61	0.57	0.65
		4-methyl-2-oxopentanoate	0.62	0.63	0.61
		alpha-hydroxyisovalerate	0.99	1.31	0.90
		butyrylcarnitine	1.46	1.57	1.31
		hydroxyisovaleroyl carnitine	1.20	1.18	1.24
		isobutyrylcarnitine	1.97	2.33	1.66
		isoleucine	0.87	0.92	0.81
		isovalerylcarnitine	1.62	1.89	1.35
		propionylcarnitine	1.74	2.11	1.42
	Aminosugars metabolism	erythronate*	1.16	1.27	1.07
Peptide	Dipeptide	alanylalanine	0.71	0.80	0.66
		gamma-glutamylvaline	0.95	1.03	0.90
	Dipeptide derivative	anserine	1.53	1.77	1.42
	g-glutamyl	gamma-glutamylglutamate	1.39	1.17	1.60
		gamma-glutamylmethionine*	1.66	1.93	1.49
		gamma-glutamylphenylalanine	1.54	1.64	1.45
		gamma-glutamylthreonine*	1.14	1.12	1.16
		gamma-glutamyltryptophan	1.31	1.21	1.45
		gamma-glutamyltyrosine	1.58	1.65	1.52
Nucleotide	Purine metabolism, (hypo)xanthine/inosine containing	inosine	0.32	0.52	0.28
	Purine metabolism, adenine containing	1-methyladenosine	0.98	0.93	1.05
		adenosine	0.36	0.20	0.37
		adenosine 5'-monophosphate (AMP)	0.39	0.96	0.38
	Purine metabolism, guanine containing	guanosine	0.99	1.00	0.99
		guanosine 5'- monophosphate (GMP)	0.86	1.00	0.84
	Purine metabolism, urate metabolism	allantoin	1.23	1.25	1.22
		urate	1.33	1.26	1.40
	Pyrimidine metabolism, cytidine containing	2'-deoxycytidine	1.43	1.39	1.48
		cytidine	0.67	0.67	0.67
	Pyrimidine metabolism, thymine containing	thymidine	1.44	1.42	1.48
	Pyrimidine metabolism, uracil containing	5,6-dihydrouracil	1.72	2.28	1.33
		pseudouridine	1.25	1.17	1.35
		uridine	0.55	0.59	0.52
Carbohydrate	Fructose, mannose, galactose, starch, and sucrose metabolism	fructose	0.82	0.72	0.92
		mannose	0.72	0.66	0.79
	Glycolysis, gluconeogenesis, pyruvate metabolism	1,5-anhydroglucitol (1,5-AG)	0.56	0.61	0.52
		glucose	0.82	0.86	0.79
		glycerate	1.33	1.08	1.58
	Nucleotide sugars, pentose metabolism	arabitol	1.24	1.20	1.27
		ribitol	1.49	1.75	1.25
		ribulose	1.75	2.40	0.89

(*continued on next page*)

Table 1 (*continued*)

SUPER PATHWAY	SUB PATHWAY	BIOCHEMICAL	ALL KO /	KO F /	KO M /
Lipid	Bile acid metabolism	12-dehydrocholate	2.84	2.15	5.60
		beta-muricholate	2.81	2.52	3.80
		cholate	19.28	17.52	26.94
		deoxycholate	5.06	4.46	5.89
		tauro-beta-muricholate	30.85	36.17	12.80
		taurochenodeoxycholate	35.96	45.42	15.23
		taurocholate	28.37	32.98	17.20
		taurodeoxycholate	11.80	13.31	8.39
	Carnitine metabolism	3-dehydrocarnitine*	1.09	1.04	1.17
		acetylcarnitine	0.90	0.80	1.04
		carnitine	0.92	0.88	0.96
		deoxycarnitine	1.12	1.07	1.20
		hexanoylcarnitine	0.95	0.72	1.41
		oleoylcarnitine	1.05	0.98	1.28
	Essential fatty acid	dihomo-linolenate (20:3n3 or n6)	0.69	0.80	0.63
		docosahexaenoate (DHA; 22:6n3)	0.74	0.69	0.80
		docosapentaenoate (n3 DPA; 22:5n3)	0.54	0.57	0.50
		eicosapentaenoate (EPA; 20:5n3)	0.78	0.89	0.68
		linolenate [alpha or gamma; (18:3n3 or 6)]	0.75	0.70	0.80
	Fatty acid, beta-oxidation	hexanoylglycine	0.54	0.19	0.98
	Fatty acid, dicarboxylate	adipate	0.89	1.05	0.79
		azelate (nonanedioate)	0.89	0.86	0.91
		sebacate (decanedioate)	0.90	0.87	0.93
		suberate (octanedioate)	1.02	1.01	1.02
		undecanedioate	0.92	0.89	0.94
	Fatty acid, methyl ester	methyl palmitate	0.99	0.96	1.01
	Glycerolipid metabolism	glycerol	0.77	0.71	0.83
		glycerophosphorylcholine (GPC)	0.78	0.78	0.78
	Inositol metabolism	inositol 1-phosphate (I1P)	0.79	0.90	0.72
		myo-inositol	1.12	1.18	1.07
	Ketone bodies	3-hydroxybutyrate (BHBA)	0.24	0.16	0.67
	Long chain fatty acid	10-heptadecenoate (17:1n7)	0.71	0.68	0.74
		10-nonadecenoate (19:1n9)	0.57	0.51	0.65
		dihomo-linoleate (20:2n6)	0.75	0.67	0.85
		dodecanedioate	0.91	0.89	0.92
		eicosenoate (20:1n9 or 11)	0.74	0.73	0.75
		linoleate (18:2n6)	0.82	0.78	0.86
		myristate (14:0)	0.60	0.54	0.66
		myristoleate (14:1n5)	0.45	0.32	0.62
		oleate (18:1n9)	0.67	0.60	0.76
		palmitate (16:0)	0.80	0.80	0.81
		palmitoleate (16:1n7)	0.52	0.45	0.58
		stearate (18:0)	0.87	0.84	0.92
	Lysolipid	1-arachidonoylglycerophosphocholine*	0.74	0.77	0.70
		1-arachidoylglycerophosphocholine	0.94	1.46	0.74
		1-docosahexaenoylglycerophosphocholine*	0.80	0.85	0.73
		1-eicosatrienoylglycerophosphocholine*	0.63	0.78	0.49
		1-heptadecanoylglycerophosphocholine	0.87	0.85	0.95
		1-linoleoylglycerophosphoinositol*	1.48	1.80	1.24
		1-myristoylglycerophosphocholine	0.86	0.94	0.73
		1-oleoylglycerophosphate	0.96	1.03	0.92
		1-palmitoylglycerophosphate	0.90	0.93	0.88
		1-palmitoylglycerophosphocholine	0.83	0.90	0.76
		1-palmitoylglycerophosphoinositol*	1.03	0.80	1.16
		1-stearoylglycerophosphocholine	0.82	0.88	0.74
		2-linoleoylglycerophosphocholine*	0.89	1.03	0.70
		2-palmitoylglycerophosphocholine*	0.75	0.92	0.57
		2-stearoylglycerophosphocholine*	0.76	0.78	0.70
	Medium chain fatty acid	laurate (12:0)	1.03	0.90	1.25
		pelargonate (9:0)	0.98	0.98	0.99
	Monoacylglycerol	1-stearoylglycerol (1-monostearin)	1.00	1.16	0.88
	Sterol/Steroid	7-alpha-hydroxy-3-oxo-4-cholestenoate (7-Hoca)	1.12	1.13	1.09
		campesterol	0.68	1.20	0.39
		cholesterol	0.99	1.07	0.95
		corticosterone	1.87	1.94	1.72
Energy	Krebs cycle	alpha-ketoglutarate	0.55	0.66	0.46
		cis-aconitate	1.21	1.15	1.28
		citrate	1.31	1.21	1.43
		succinate	1.04	1.31	0.83
	Oxidative phosphorylation	phosphate	0.70	0.72	0.67
		pyrophosphate (PPi)	0.49	0.56	0.35
Cofactors and vitamins	Ascorbate and aldarate metabolism	ascorbate (Vitamin C)	0.56	0.80	0.37
		gulono-1,4-lactone	1.10	0.99	1.16
		threonate	1.00	0.90	1.11
	Nicotinate and nicotinamide metabolism	nicotinamide	0.55	0.63	0.46
		trigonelline (N'-methylnicotinate)	1.30	1.31	1.30
	Pantothenate and CoA metabolism	pantothenate	1.07	1.20	0.91
Xenobiotics	Benzoate metabolism	4-ethylphenylsulfate	0.51	1.03	0.03
		4-vinylphenol sulfate	2.42	3.31	1.73
		catechol sulfate	1.57	2.21	1.11
	Chemical	methyl-alpha-glucopyranoside	0.30	0.24	0.33
	Food component/Plant	daidzein	3.26	3.37	3.21
	Sugar, sugar substitute, starch	erythritol	1.16	1.24	1.11

analysis not only explored the interplay between the gut microbiome and host metabolism but also characterized sex different metabolic processes. Table 1 lists overall metabolic changes observed between female vs male ARE-Del mice compared to control littermates at 4 weeks of age as described in the methods section. Each value represents the relative expression ratio transformed to log2 scale, and significantly ($p < 0.05$) up- or down-regulated changes are marked as a red or green color, respectively. Notable changes in both male and female homozygous ARE-Del mice included tryptophan metabolism, bile acid and long-chain lipid metabolism, and gamma-glutamyl transferred peptides. Principal component analysis (PCA) revealed robust sex differences between male vs female in both homozygous ARE-Del mice and control littermates (Fig. 3A). Genotypes also strongly affected metabolic profiling, while genotype difference was relatively greater in female than male mice. In detail, changes of identified metabolites in male and female homozygous ARE-Del mice were compared by the positive correlation of a scatter plot (Fig. 3B). Strong sex-difference was detectable in three notable areas (marked as red circles) based on correlated metabolites. *p*-cresol sulfate and 4-ethylphenylsulfate, known as microbial metabolites [19,20], were more significantly altered in male than female ARE-Del mice. Other two notable areas include metabolites associated with fatty acid oxidation (FAO) and tauro-conjugated bile acids. As overall fold changes were stronger in female ARE-Del mice, mostly located between +1 and −1 relative fold ratio (dotted lines), metabolites with sex-differences are shown in Fig. 3C. Robust sex-differences were visible in amino acid metabolisms including glycine, phenylalanine, tyrosine, and tryptophan metabolism as well as urea cycle. Considering that most of these metabolites contain an aromatic ring, sex-different metabolic processes are likely involved in nuclear receptor-mediated metabolic pathways such as mitochondrial fatty acid oxidation.

As shown in Fig. 3D and E, the basal expression levels of hexanoylglycine and 3-hydroxybutyrate were higher in female wild type mice than male mice. Furthermore, the basal level of hexanoylglycine was dramatically suppressed only in female homozygous ARE-Del mice. Not only mitochondiral fatty acid oxidation but other mitochondrial energy metabolic processes were significantly altered with an observed sex-difference. Metabolites linked to these pathways include female-specific increases of succinate and ribulose in homozygous ARE-Del mice (Supplemental Figs. 2A and 2B). Analysis of bile acid composition in homozygous ARE-Del mice demonstrated that tauro-conjugated bile acids including tauro-beta muricholate, taurochenodeoxycholate, taurocholate, and taurodeoxycholate were higher in female than male homozygous ARE-Del mice, while non-conjugated bile acids such as deoxycholate, cholate, beta-muricholate are higher in male homozygous ARE-Del mice (Fig. 3F). Further, we compared the ratio of each tauro-conjugated vs non-conjugated bile acid and the most notable difference was found in tauro-beta-muricholate, a natural FXR antagonist, between male and female ARE-Del mice (Fig. 3G).

3.4. Early alteration of B cell and nuclear signaling in the peripheral blood are correlated with later inflammation in the kidney in female homozygous ARE-Del mice

As noted, the cecal microbiome was altered in homozygous ARE-Del mice, of which changes were much stonger when compared to the heterozygotes than any sex-differences in these mice. Furthermore, pathological and serological phenotypes such as loss of marginal zone B cells and autoantibody production are distinctive between homozygous and heterozygous ARE-Del mice beyond any sex-differences [7]. Thus, we compared gene expression profiles in female homozygous vs heterozygous ARE-Del mice, at different ages and in different tissues to characterize mechanistic differences. In Fig. 4A, a PCA plot shows clusters of gene expression data from all 218 samples, as described in the methods section, based on their similarity. Gene expression profiles in each tissue were distinctive and separated from other tissues with a mild effect of age, thus we further analyzed differentially expressed (DE) genes of female homozygous and heterozygous ARE-Del mice compared to control littermates in each tissue as shown in Fig. 4B. The statistical analysis was performed using Partek Genomics Suite 6.6 and the number of DE genes of female homozygous and heterozygous ARE-Del mice in each tissue were generated and compared to control littermates with a p-value threshold of 0.05 and ± 2 fold change cut-off. Up-regulated genes (a fold change ≥2 with a p-value < 0.05) were marked with an orange color, and down-regulated genes (a fold change ≤ -2 with a p-value < 0.05) were marked with a blue color, respectively. Among these changes, it was notable that DE genes were highly increased from an early age at 3 weeks, specifically in the blood (PBMCs) from both female homozygous and heterozygous ARE-Del mice.

Although the number of DE genes indicate how genes in each tissue rapidly responded over a time period, mechanism-based analysis also gives crucial information to understand how these DE genes are meaningfully connected with mechanistic processes for pathogenic development. Fig. 4C presents that the number of significantly changed canonical pathways ($p < 0.05$) of either up- or down-regulated genes in PBMCs, spleen, and kidney over age, analyzed by Ingenuity pathway analysis (IPA). Here, we specifically analyzed differential pathways between female homozygous vs heterozygous ARE-Del mice to characterize homozygous-specific mechanistic changes which can be connected with homozygous-specific microbial alteration.

As shown in Fig. 4D, the top three canonical pathways for up- or downregulated genes in the PBMCs and spleen are listed (a-d) and top ten canonical pathways for upregulated genes in the kidney are also listed (e-f) in order. Overally, notable changes in PBMCs and spleen were detectable at 3 weeks of age and particularly include macrophage activation (data not shown here) and impaired B cell signaling. Furthermore a sequential increase of T cell signaling was detectable in the kidney from 6 weeks of age, implying that early changes in the peripheral blood immune cells impact later inflammatory responses in the kidney. The highest top canonical pathways in PBMCs reflected the finding that nuclear receptor FXR/RXR and LXR/RXR signaling was increased at 3 weeks (a) and oppositely suppressed at 12 weeks (c). A similar pattern was detected in PPAR signaling, driven by gene set enrichment analysis (GSEA) (Fig. 4E). A set of genes related to PPAR signaling obtained from GSEA databases was increased at 3 weeks of age and later suppressed at 12 weeks of age in female homozygous ARE-Del mice compared to control littermates. The kidney had highly up-regulated canonical pathways that regulate the development of CD4 T helper cells from 6 weeks of age (e-f). As mentioned before, another remarkable gene expression change in PBMCs was suppression of B cell receptor signaling, detectable at 3 weeks of age (b). A similar but weaker pattern was detectable in the spleen (d) but not in the thymus. Using flow cytometry analysis, a subpopulation of B cells in the spleen from female homozygous ARE-Del mice and control littermates at 4 weeks of age were analyzed (Supplemental Fig. 3A). Given that immature B cells ($CD21^{low}CD23^{low}$) were higher in ARE-Del mice, while FO ($CD21^{int}CD23^{int}$) and marginal zone (MZ) B cells ($CD21^{high}CD23^{low}$) were lower in ARE-Del mice compared to control littermates, it is likely that early suppressed B cell signaling in the gene expression pattern results in impaired B cell differentiation in the secondary lymphoid organs.

A.

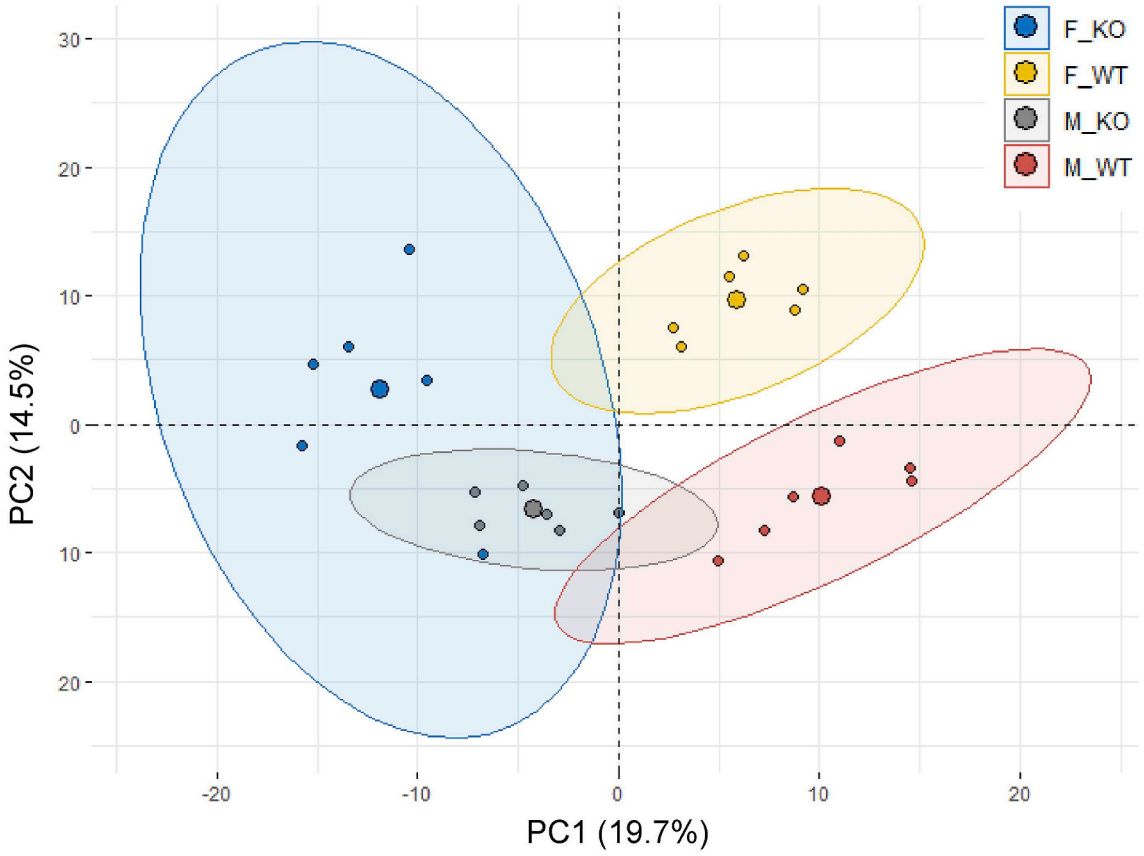

B.

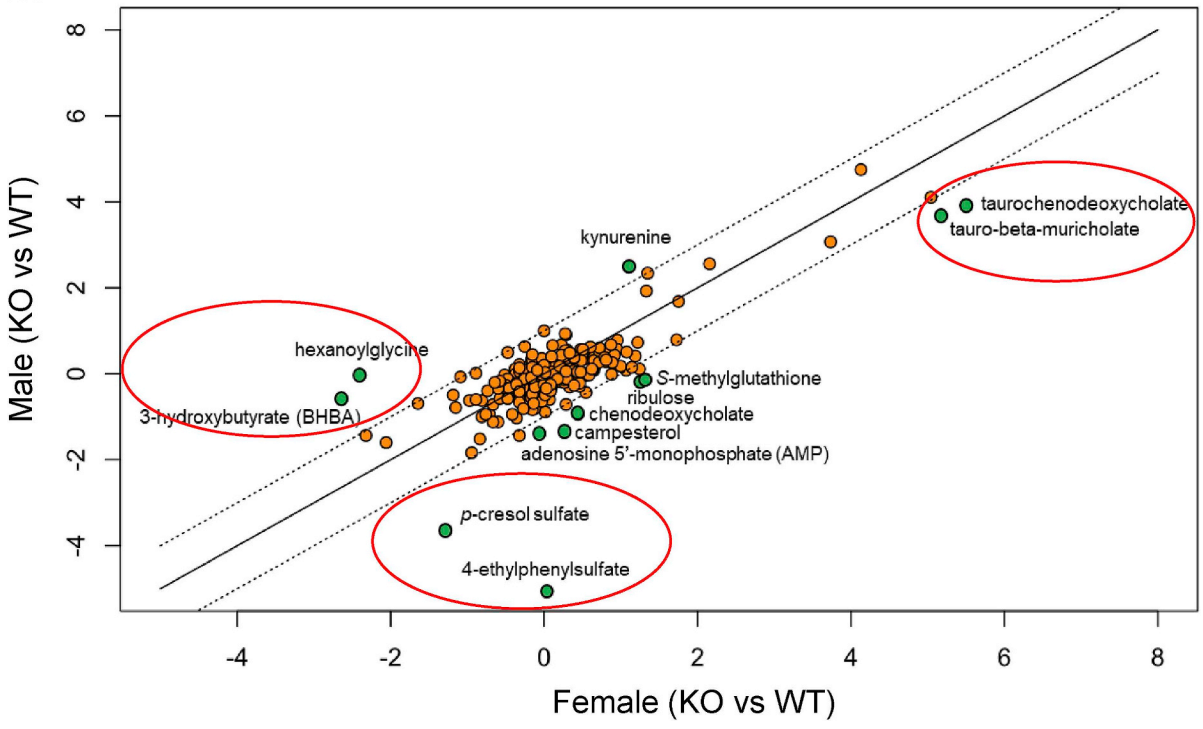

(caption on next page)

Fig. 3. Sex-specific metabolite profiles in homozygous ARE-Del mice. (A) A PCA plot of the metabolites in male or female homozygous ARE-Del mice vs control littermates. (B) Scatter plot showing the relationship between overall metabolites (Log2 fold changes) from male or female homozygous ARE-Del mice vs control littermates. Dotted lines point relatively one fold up or down-regulated directions between male vs female homozygous ARE-Del mice. (C) Heatmap of differentially expressed metabolites ($p < 0.05$), which were selected from Figure B and presented by log2 fold change. ($p < 0.05$). (D–E) FAO related metabolites (hexanoylglycine and 3-hydroxybutyrate) in male and female homozygous ARE-Del mice compared to control littermates (each group, n = 4–6). Statistical analysis is performed by Mann Whitney test (**$p < 0.001$). Sex-different bile acid composition in male and female homozygous ARE-Del mice (F–G). (F) The relative ratio of bile acids was calculated by comparison of fold changes between male or female homozygous ARE-Del vs control littermates. (G) The relative ratio of tauro-conjugated vs unconjugated bile acids in male and female ARE-Del −/− mice. CA; cholate, TCA; taurocholate, DCA; deoxycholate, TDCA; taurodeoxycholate, βMCA; beta-muricholate, TβMCA; tauro-beta-muricholate, CDCA; chenodeoxycholate, TCDCA; taurochenodeoxycholate.

3.5. mTOR-autophagy pathway is dysregulated in macrophages at early ages, as an initial pathogenic mechanism in female homozygous ARE-Del mice

Given that macrophage depletion by CLL significantly reduces splenic MZB cells and increases ANA production, we hypothesized that functional alteration of macrophage at early ages plays a critical role in B cell differentiation in secondary lymphoid organs and development of autoantibodies. To predict each activation level of peripheral blood immune cells, we utilized K-means clustering to sort genes based on patterns of gene expression (Supplemental Fig. 4). We clustered into 20 gene sets based on their expression patterns over time and analyzed the most target cells and tissues in each cluster, according to Mouse Gene Atlas. Consistent with pathway analysis, the pattern with early suppression corresponded to follicular B cell signaling (Supplemental Fig. 4A). In contrast, the pattern of gene expression revealed early activation as well as persistent activation over time that was consistent with activated macrophage signaling (Supplemental Figs. 4B and 4C), suggesting that early altered macrophage function is critical for the disease progression. In addition, dendritic cell signaling gradually increased (Supplemental Fig. 4D), indicating that chronic DC activation corresponds to pathological development of autoimmune diseases. Based on our observations, we next focused on evaluating autophagy, which is known as a critical pathway in macrophages, regulating phagocytosis, antigen processing, metabolic processes and inflammatory responses. First, we examined mTOR signaling and autophagy-related genes depending on the age in homozygous ARE-Del mice (Fig. 5A). As early as 3 weeks, genes regulating mTOR signaling and autophagy were most affected and dysregulated. To evaluate the dysregulated function of these pathways, we isolated peripheral macrophages and developed bone-marrow derived macrophages from female homozygous ARE-Del mice, in order to examine the formation of autophagosomes in the presence or absence of the mTOR inhibitor, rapamycin (Fig. 5B and C). In Fig. 5B, bone-marrow derived macrophages were treated with rapamycin with or without pre-treatment with bafilomycin to inhibit degradation of LC3-II. LC3-II accumulated in wild type mice upon treatment of rapamycin, indicating increased autophagy processes upon suppression of mTOR signaling. However, the LC3-II complex was not increased in cells from homozygous ARE-Del mice under the same conditions. We further confirmed the autophagosome formation using Cyto-ID staining (Fig. 5C). Upon treatment with Rapamycin, autophagosomes stained by green-fluorescent Cyto-ID were increased in bone-marrow derived macrophages from wild type mice but not homozygous ARE-Del mice, whereas the basal level of autophagosomes slightly increased in macrophages from homozygous ARE-Del mice compared to control mice.

To characterize autophagy function in macrophages at a systemic level, the expression level of macrophage marker genes, including Marco and Siglec1, were analyzed in blood and tissues over time. They were highly upregulated in the blood and kidneys at 3 weeks of age, with such activation being sustained or gradually decreased with age (Fig. 5D). Utilizing pathway analysis, the data indicates that female homozygous ARE-Del mice, as compared to heterozygotes, have more profound alterations of phagosome formation and maturation, and oxidative phosphorylation at 3 weeks of age (Supplemental Fig. 5). Consistently, the gene expression profiles support the model that genes involved in autophagy process were down-regulated in kidney from homozygous ARE-Del mice, while this pathways were not significantly changed in the kidney from heterozygous mice (Fig. 5E), thus indicating that levels of IFN-γ can have different effects on host physiology.

3.6. Abnormal thymic B cell development and its effect on central T cell tolerance in female homozygous ARE-Del mice

DE gene profiles showed that there was a significant increase of gene expression in the thymus at 12 weeks of age specifically in homozygous ARE-Del mice (Fig. 4B). Although pathway analysis did not characterize well top canonical pathways in the thymus, possibly due to the specificity of thymic gene expression, we noticed that thymic B cell markers were changed with a similar pattern of DE gene profiles. Furthermore, CD 19, a surface marker for B cells, gradually increased in the thymus with age, but not other tissues in female homozygous ARE-Del mice (Fig. 6A). Seeing that early B cell receptor signaling was highly suppressed in PBMCs, we further compared expression levels of other B cell markers and MHC class II molecules in PBMCs and the thymus depending on the genotype at 3, 6 and 12 weeks of age (Fig. 6B). Correlated with an early suppressed B cell response in PBMCs, the expression of B cell markers and MHC II molecules are much higher in the thymus from female homozygous ARE-Del mice at later ages. Particularly, AIRE, CD40, and CD80 increased along with MHC class II molecules at 12 weeks of age, indicating that abnormal development of thymic B cells may affect central T cell tolerance [21]. We further confirmed the increase of B cell marker (B220) in the thymus by immunohistochemistry (Supplemental Fig. 3B). In the integrative analysis of miRNA and mRNA profiles in the thymus, performed by IPA, we noticed that expression levels of significantly changed ($p < 0.05$) miRNA were persistently suppressed and those miRNA that targeted 73 genes were correspondingly increased, matched by age (12 weeks old), in female homozygous ARE-Del mice (Supplemental Table 1). The most significantly changed miRNA ($p < 0.05$, fold change cut offs $\pm$ 1.5) and target mRNAs were listed in Fig. 6C. We performed pathway analysis of 73 miRNA-mRNA target genes by IPA and top canonical pathways include communication between innate and adaptive immune cells; altered T cell and B cell signaling in rheumatoid arthritis; systemic lupus erythematosus signaling (Fig. 6D).

4. Discussion

Emerging studies have focused on the interaction between the gut microbiome alteration (referred as gut dysbiosis hereafter), chronic inflammation and autoimmune diseases [22–27]. Although the association of chronic inflammation with gut dysbiosis and autoimmune diseases is well recognized, the mechanistic interactions are not well

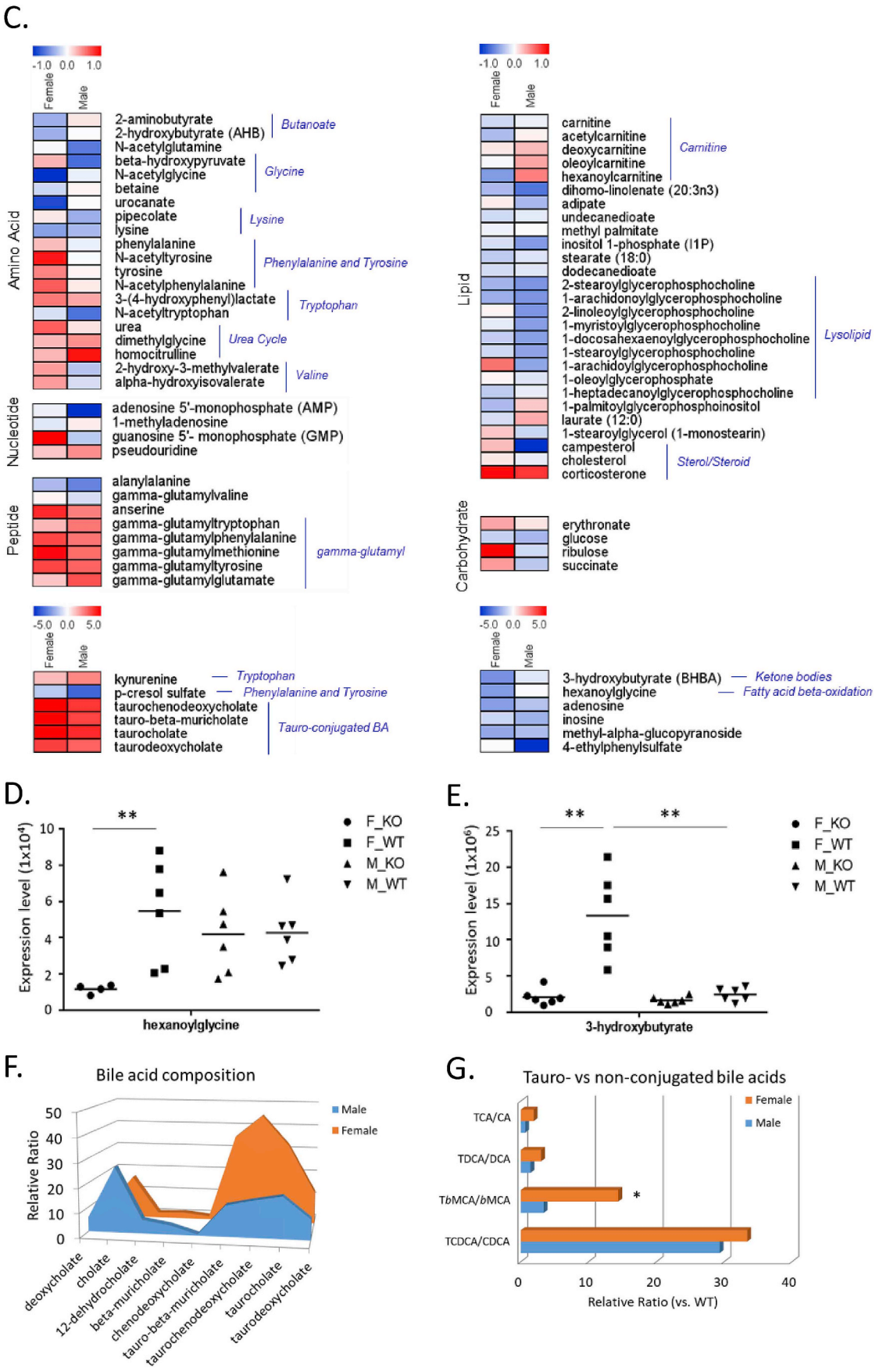

Fig. 3. (*continued*)

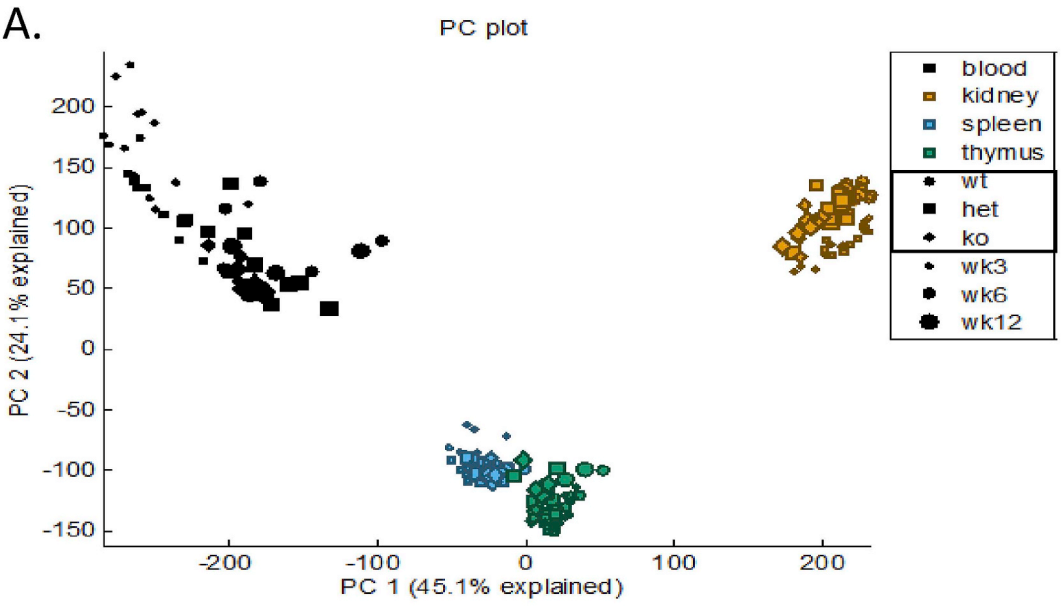

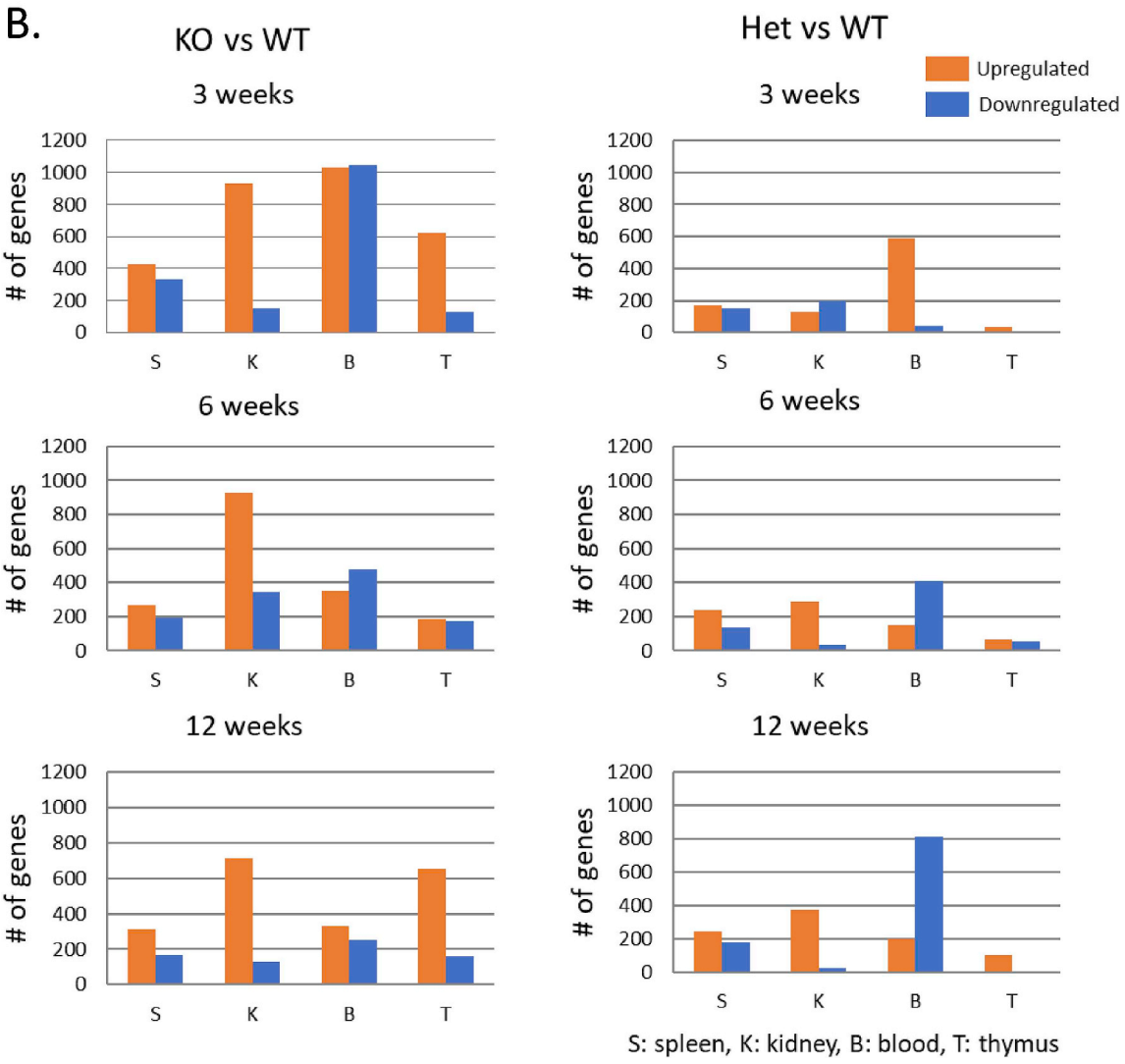

(caption on next page)

Fig. 4. Overall age- and tissue-dependent gene expression profiles in female homozygous and heterozygous ARE-Del mice with control littermates. (A) A PCA plot of overall gene expression in blood, kidney, spleen, and thymus at 3, 6, 12 weeks in homozygous and heterozygous ARE-Del mice with control littermates. (B) Comparison of upregulated or downregulated genes in blood, spleen, thymus, and kidney from homozygous and heterozygous ARE-Del mice compared to control littermates at 3, 6, 12 wks. The total height of each bar indicates the number of genes (orange bar; upregulated genes, blue bar; downregulated genes). S; spleen, K; kidney, B; blood, T; thymus. (C) Number of canonical pathways in homozygous ARE-Del mice compared to heterozygous ARE-Del mice in blood, spleen, and kidney at 3, 6, and 12 weeks old. The total height of each bar indicates the number of significant canonical pathways derived from upregulated (orange) or downregulated (blue) genes in female homozygous ARE-Del mice compared to heterozygotes. (D) The significant number of canonical pathways from Fig. 5A was calculated by –log (p-value) less than 1.5 (relative to p-value $<$ 0.05). Ratio (red line) refers to the number of genes from the data set divided by the total number of genes according to the IPA knowledge base. a-f; representative top canonical pathways ordered from the highest one in each group. (E) GSEA plots of PPAR signaling in the blood with a comparison between 3 and 12 weeks in female homozygous ARE-Del mice. PPAR signaling gene set was derived from the GSEA database, and enrichment was defined by normalized enrichment score (NES), false discovery rate (FDR) *q*-value. (For interpretation of the references to color in this figure legend, the reader is referred to the Web version of this article.)

understood. Strikingly, our data on homo, hetero and WT mice in diversity and richness of that cecal microbiome (Fig. 1A) suggests that chronic expression of IFN-γ has a threshold level to break gut homeostasis. Moreover, gut dysbiosis occurred at an early age and is systemically correlated with other pathological mechanistic features found in homozygous ARE-Del mice. In view of the fact that IFN-γ is a critical regulator of gut homeostasis against viral and microbial infection [28], our data indicate that low but chronic expression of IFN-γ has a detrimental role in gut homeostasis depending on the expression level and is pivotal to the pathogenic development of autoimmune diseases.

In addition to gut microbial changes, the metabolic profiles such as amino acid metabolites reflected strong differences between sexes. Consistent with this finding, recent evidence suggests that amino acid metabolism is a major sex-discriminating factor in the liver during fasting in order to provide a fuel to maintain lipid synthesis in mice [29]. We further focused on both sex- and genotype-dependent metabolic processes and found that β-hydroxybutyrate and hexanoylglycine were among the most affected metabolites by both processes (Fig. 3B). Given that β-hydroxybutyrate, known as 3-hydroxybutyrate (BHBA), is a indicator for the FAO rate during fasting [30] and hexanoglycine is also involved in FAO [31], it is expected that FAO plays a critical role in the pathogenetic development of immune responses. Furthermore, the level of acylcarnitine is clearly different between male and female ARE-Del mice. Carnitine is an essential transporter of fatty acid into mitochondria via conversion into acylcarnitine for subsequent mitochondrial fatty acid oxidation in human and mice [32]. As the level of circulating acylcarnitine is positively correlated with the rate of FAO upon fasting condition [33], the different expression level of circulating acylcarnitine in male vs female ARE-Del mice under fasting conditions can reflect the activated status of FAO. Due to the fact that FAO is a key metabolic process to modulate inflammatory responses [34,35], and is modulated by nuclear receptors such as peroxide proliferator-activated receptors (PPARs) and liver X receptors (LXRs), interacting with estrogen receptors [36], these observations point to the significance of nuclear receptor signaling in the development of sex-different inflammatory responses via modulation of lipid metabolic processes in ARE-Del mice.

Here we featured that composition of serum bile acids was dramatically changed in homozygous ARE-Del as compared to control littermates, particularly in the tauro-conjugated bile acid composition. Female mice also have a higher induction than male mice. This feature is consistent with our previous report demonstrating that the increased level of serum total bile acids (TBA) was significantly detectable in homozygous but not heterozygous ARE-Del mice, and this pattern is also female-biased. On the basis that the gut microbiome has a critical role in the bile acid metabolism in the gut-liver axis, particularly through nuclear receptor FXR, we further focus on the connection between FXR and bile acid composition being linked to the gut microbiome alteration. Interestingly, the conjugated vs non-conjugated ratio of tauro-β-muricholic acid noticeably increased in female ARE-Del mice (Fig. 3G). Tauro-β-muricholic acid is recently identified as a natural competitive and reversible antagonist of FXR [37] and is known to be controlled by the gut microbiome, as shown by the observation that the level of tauro-β-muricholic acid is approximately 10 times higher in bile from germfree than from conventional rats [38]. Since bile acid synthesis is under negative feedback control through activation of FXR, the interplay of the gut microbiome in reducing tauro-β-muricholic acid (a FXR antagonist in this case) can have profound effects on bile acid synthesis via FXR [39,40]. Given that gene expression profiles of FXR signaling were clearly suppressed in the liver as well as in the PBMCs over time period in homozygous ARE-Del mice and predominantly in female mice, our data indicate that FXR plays a critical role in bile acid and lipid metabolism interacting with the gut microbiome in response to chronic expression of IFNγ, eventually affects liver inflammatory responses and pathological progression of PBC.

Other additional data also support the hypothesis that the gut microbiota modulates host metabolites, which further interact with nuclear receptor signaling and modulate inflammatory responses in ARE-Del mice. One of the notable changes is that tryptophan metabolism is highly altered in homozygous ARE-Del mice, including upregulation of kynurenine and indolelactate as well as suppression of serotonin, N-acetyl tryptophan, and tryptophan (Table 1). Kynurenine is an endogenous ligand of the aryl hydrocarbon receptor (AhR) and indolelactic acid is a bacterial metabolite as a ligand of AhR [41]. Emerging evidence suggests that AhR is a critical modulator for inflammatory responses and intestinal immunity [42,43] and its activity is linked to several autoimmune diseases [44,45]. As additional evidence, the plasma level of succinate was differentially changed between male and female ARE-Del mice compared to control littermates (Supplemental Fig. 2A). Succinate, involved in the TCA cycle, is known as a metabolic signal in inflammation. Circulating succinate levels increase upon deletion of nuclear receptor4 group A1 (Nr4a1) and consequently induce Th1/Th17 differentiation [46–48]. Regarding that obesity-associated gut microbiota increases circulating levels of succinate [49] and female Nr4a1 deficient mice show increased susceptibility to high fat diet-induced obesity [50], sex-different circulating levels of succinate can be a consequence of the sensitivity to the suppression of Nr4a1. Taken together, our data suggest that nuclear receptors are integrative modulators of lipid metabolism, inflammation, and gut microbial homeostasis as a result of chronic expression of IFN-γ.

Given that nuclear receptors crosstalk with sex-hormone signaling pathways, this feature is also crucial for sex-specific pathogenesis in autoimmune diseases. Particularly, PPARs play a central role in female-biased inflammation and autoimmunity depending on the interaction with sex hormones in immune cells [51,52], and IFN-γ negatively regulate PPAR gamma expression at the transcription level [53]. Notably, gene expression profiling shows that FXR, LXR and PPAR signaling pathways are among the top canonical pathways detected from

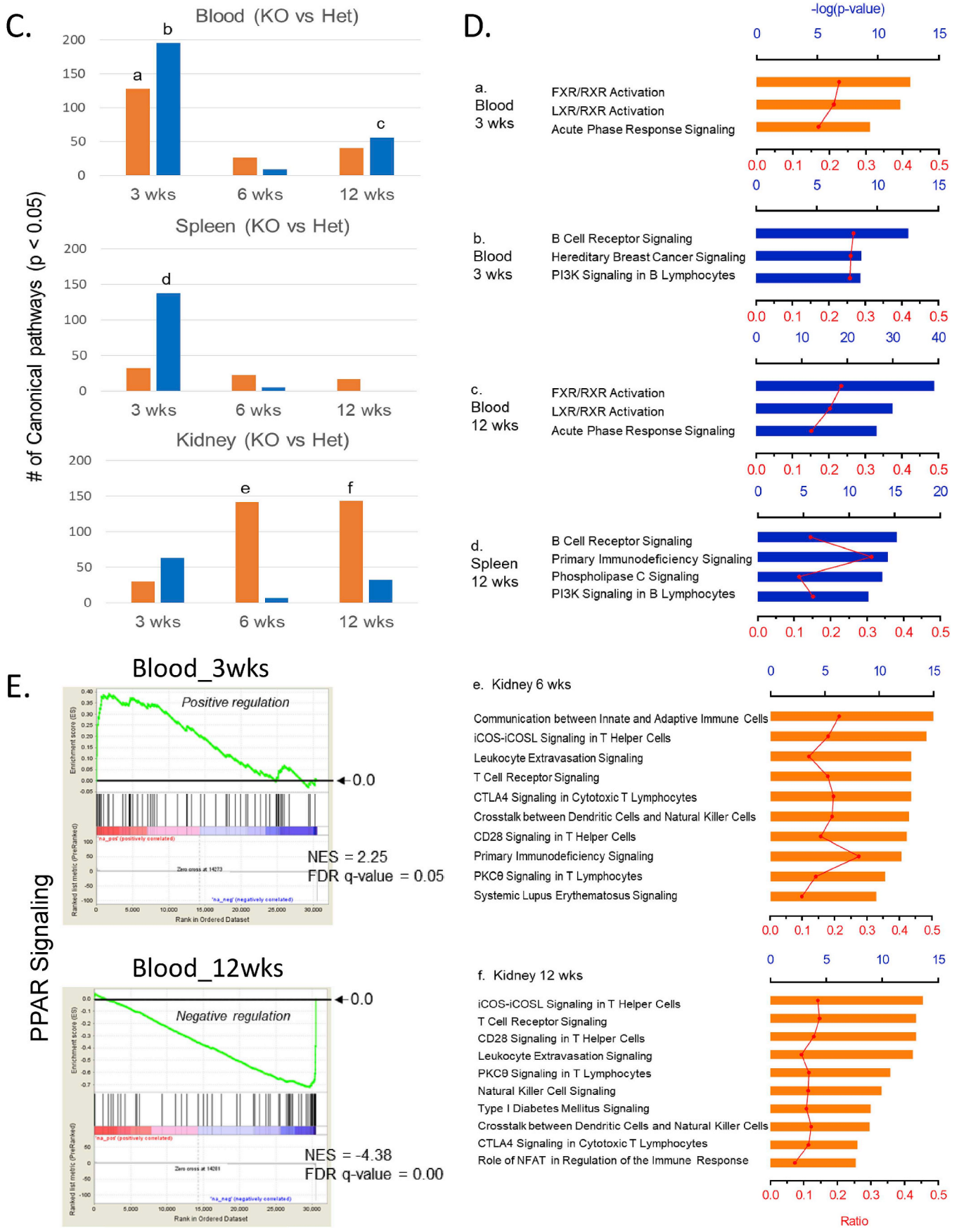

Fig. 4. (*continued*)

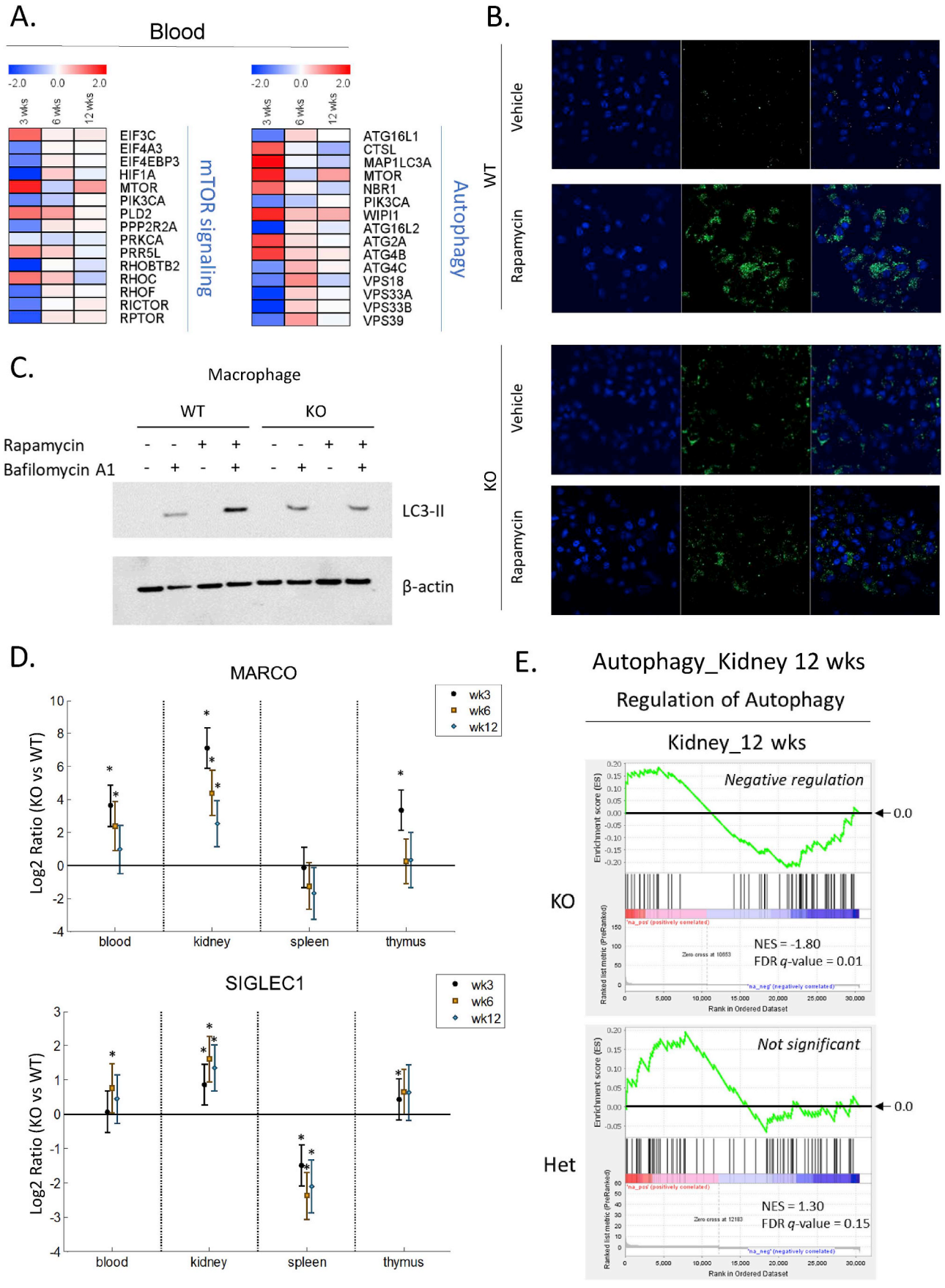

(caption on next page)

Fig. 5. Dysregulated autophagy process from female homozygous ARE-Del mice. (A) Heat map of gene expression profiles in the blood related to the mTOR signaling pathway and the autophagy process in female homozygous ARE-Del mice compared to heterozygotes. (B) Representative images of autophagosome formation after rapamycin treatment in bone-marrow derived macrophages from female homozygous ARE-Del mice and control wild type mice. Both normal control and treated cells were stained with Cyto-ID® green dye and Hoechst 33,342, followed by the manufacturer's protocol. (C) Immunoblotting to detect the accumulation of LC3-II upon treatment of rapamycin (3 μM, 2 h) with or without pre-treatment of bafilomycin A1 (50 nM, 30 min prior to rapamycin). (D) Gene expression levels of macrophage markers (Marco and Siglec1) comparing homozygous ARE Del mice to control littermates in blood, kidney, spleen, and thymus according to 3, 6, and 12 weeks of age. Statistical analysis is performed by *t*-test, *P $<$ 0.05. (E) GSEA plots of positive regulation of the autophagy process in the kidney from homozygous and heterozygous ARE-Del mice at 12 weeks old. (For interpretation of the references to color in this figure legend, the reader is referred to the Web version of this article.)

the early stage of homozygous ARE Del mice (Fig. 4D). As suggested that there is a reciprocal negative crosstalk between LXRs and IFN-γ-stimulated STAT1-dependent transcription [54], and IFN-γ-stimulated STAT1 activation suppresses FXR transcription [55] in macrophages, it is expected that IFN-γ negatively modulates FXR, LXRs, and PPARs expression via the transcriptional suppression of these nuclear receptors. In addition, sex steroid hormones modulate gut microbiota-host interaction and nuclear receptors regulate intestinal inflammatory responses [56,57]. Our observations support the hypotheses that a sex-different microbial alteration can interact with host nuclear receptor signaling and vice versa. Thereby, IFN-γ targets a variety of nuclear receptor signaling and modulates nuclear receptor signaling directly or indirectly through microbial alterations, resulting in both genotype-as well as sex-biased pathogenesis in autoimmune diseases.

Homozygous ARE-Del mice specifically have a decrease of the splenic B cell population [9] and the loss of splenic marginal zone (MZ) macrophages and B cells [7]. Moreover, the loss of MZBs and anti-nuclear antibody (ANA) are significantly increased by CLL treatment in heterozygous ARE-Del mice. Given that marginal zone macrophages (MZMs) are required for antigen capture by MZBs [58] and depletion of macrophages by CLL treatment suppresses B cell migration to the follicular perimeter, resulting in the loss of MZBs [59], the current findings support the concept that the antigen-presentation pathways in macrophages are essential for B cell migration and differentiation. The uptake of liposomes is targeted by the mononuclear phagocytic system (MPS), particularly macrophages [60], and liposomal clodronate induces apoptosis when it is released within the phagocytic cells [61]. Regarding that phagocytosis is closely linked to autophagy in its regulatory mechanisms [62,63], our data reveal that dysregulated autophagy plays a central role in impaired early B cell development and differentiation. Autophagy, a conserved bulk-degradation process of intracellular or extracellular components, centrally regulates antigen presentation and inflammation [64,65], and polymorphisms of autophagy-related genes have been associated with major autoimmune diseases such as SLE and RA [66,67] and inflammatory bowel disease, contributing to gut microbial homeostasis [68]. Consistent with these findings, deletion of autophagy-related genes (*Atg5*) dramatically altered the composition of the gut microbiota in a murine model [69]. Thus, we believe that the dysregulated autophagy process, particularly in macrophages, has a mechanistic role in the breakdown of B cell self-tolerance mechanisms as well as gut dysbiosis.

We previously reported that adoptive transfer of CD T cells from ARE-Del mice into wild type mice markedly increased pathological phenotypes of PBC as well as the development of germinal center B cells [8,9], indicating that autoreactive T lymphocytes are key players in autoimmune diseases in ARE-Del mice. In this aspect, we further focus on the immune response in the thymus of homozygous and heterozygous ARE-Del mice. According to the recent report that peripheral B cells migrated to the thymus upon receiving CD40 signaling in the context of cognate interaction with $CD4^+$ T cells and as such can express AIRE and upregulate MHC Class II and CD80 expression [21], our findings imply that B cells, that migrated from the peripheral to thymus can present self-antigens and enhance central T cell tolerance induction. Therefore, our data provides a new insight of how early abnormal macrophage and B cell signaling can affect T cell signaling in the thymus which can break central T cell tolerance sequentially.

In conclusion, we illustrate how these mechanistic features, resulting from chronic IFN-γ expression, interact with each other at both system cellular levels to break immune tolerance (Supplemental Fig. 6). Considering that GC B cells are critical for ANA production in lupus-prone mice [70] and homozygous ARE-Del mice have strongly biased GC B cell development [9], understanding the mechanisms to induce GC B cell-dependent autoantibodies will be pivotal for discriminating how host immune system is differently impacted by the modest different expression level of IFN-γ (Supplemental Fig. 6A). Although IFN-γ interplays with Type I IFNs that are critical for sex- and genotype-dependent pathological development in ARE-Del mice [9], it is not well understood how IFN-γ increases Type I IFN signaling. According to our findings, we can derive a hypothetical mechanism of how IFN-γ regulates Type I IFNs, thus interfering with autophagy and nuclear receptor signaling at a cellular level (Supplemental Fig. 6B). Given that autophagy intersects with Type I and II IFNs and has a suppressive role in Type I IFN activation [71], dysregulated autophagy may play a critical role in Type I IFN production in ARE-Del mice. In support of this hypothesis, abrogation of autophagy induces Type I IFN production as a result of impaired DNA-stimulated STING degradation [72,73]. Considering the fact that nuclear receptors of PPARα and FXR oppositely modulate FAO as well as autophagy depending on nutrient status in the liver [74,75] and suppression of PPARγ, LXRs, and RXR signaling by IFN-γ increases intracellular accumulation of cholesterol [76], we hypothesize that suppression of nuclear receptor signaling produces Type I IFNs via altered autophagy and lipid metabolism in ARE-Del mice.

In summary, this study illustrates the etiopathological mechanisms how low but chronic IFN-γ leads to autoimmunity, particularly via host-gut microbiota and metabolic interactions. Interestingly, distinctive mechanistic features induced by differential expression level of IFN-γ as well as sex-specific changes converge into a variety of nuclear receptor signaling pathways, suggesting that nuclear receptor activities are critical to modulate immune responses resulting in the development of autoimmune diseases. Our data also highlight how chronic IFN-γ expression mechanistically reflects chronic inflammation-mediated autoimmune diseases, and as such may be a relevant murine model of chronic inflammation in humans.

Author statement

Heekyong R. Bae: Conceptualization, Performed described experiments, Multi-omics data analysis and Visualization, Writing-original draft; Patrick S.C. Leung: Conceptualization, Experimental design, Writing-original draft; Deborah L. Hodge: Performed described experiments; John M. Fenimore: Performed described experiments; Seon-Min Jeon: Conceptualization; Vishal Thovarai: Formal microbiome data analysis; Amiran Dzutsev: Formal microbiome data analysis; Andrew A. Welcher: Formal microarray data analysis; Michael Boedigheimer:

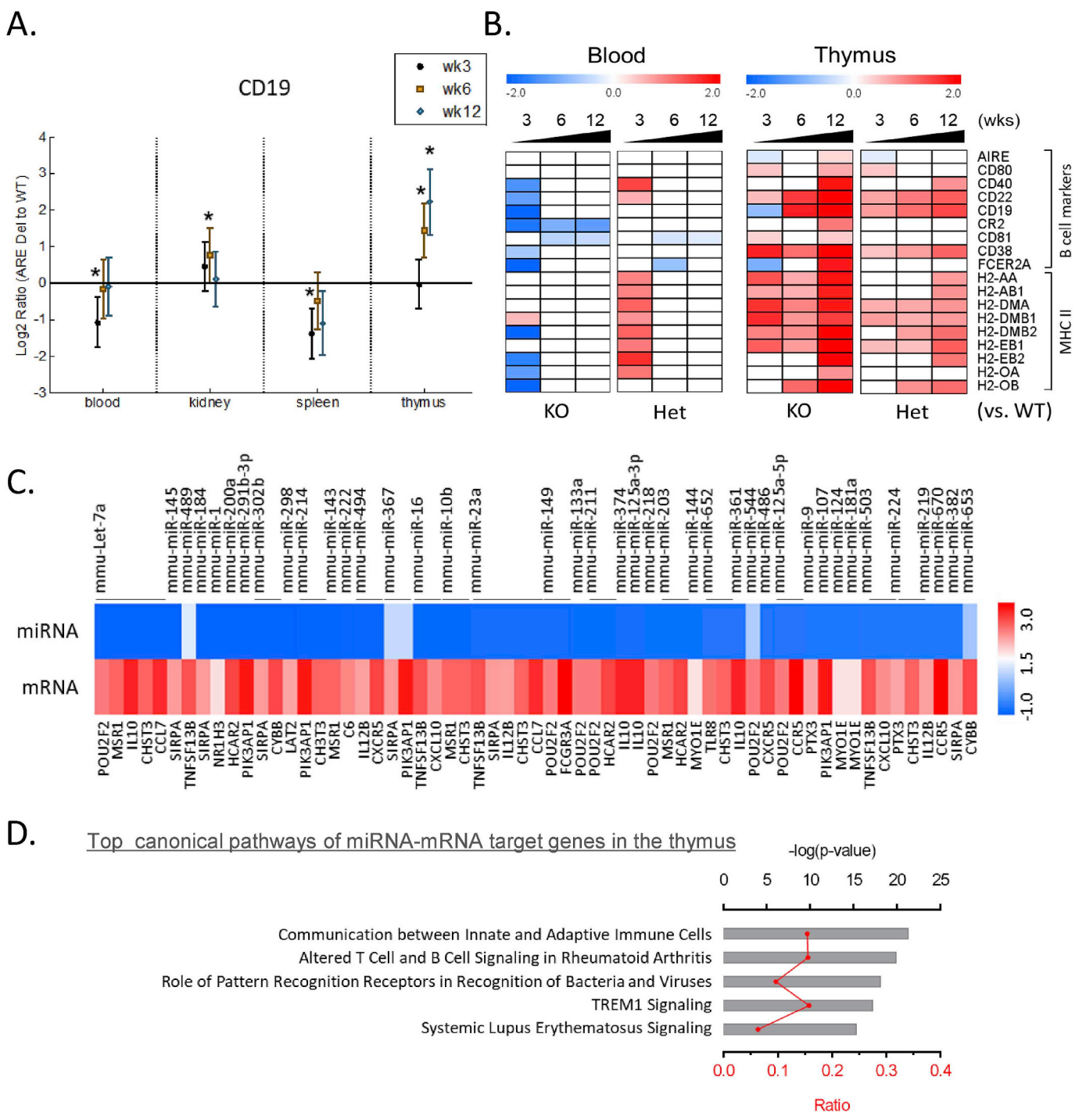

Fig. 6. Correlation between early loss of peripheral B cells and late increase of thymic B cells. (A) Gene expression levels of CD19 comparing homozygous ARE Del mice to control littermates in the PBMCs, kidney, spleen, and thymus at 3, 6, and 12 weeks old. Statistical analysis is performed by *t*-test, *P $<$ 0.05. (B) Heat map of genes for B cell markers and MHC II molecules in PBMCs and thymus according to ages in female homozygous and heterozygous ARE-Del mice compared to control littermates. (C) Heat map of miRNA-mRNA target genes in the thymus. Significantly changed microRNAs in the thymus were selected by p-value ($p < 0.05$) and fold changes (fold change threshold ± 1.5). Target genes (21 genes without overlapping) were identified by integration of miRNAs and mRNAs, which significantly changed in the thymus at 12 weeks of age, using the IPA's miRNA target filter. (D) Top canonical pathways of significantly chanted miRNA-mRNA target genes were analyzed by -log (p-value) and ratio according to IPA. Red shading indicates an increase, green shading indicates a decrease. (For interpretation of the references to color in this figure legend, the reader is referred to the Web version of this article.)

Formal microarray data analysis; Michael A. Damore: Formal microarray data analysis; Myung-Sook Choi: Critical feedback on experimental design; Richard A. Fravell: Critical feedback on experimental design; Giorgio Trinchieri: Critical feedback on data evaluation and interpretation; M. Eric Gershwin: Conceptualization, Supervision, Writing-reviewing and Editing; Howard A. Young: Conceptualization, Supervision, Writing-reviewing and Editing.

Acknowledgments

We thank Ziaur Rahman and Ogyi Park for their comments on the manuscript. We thank CCR Collaborative Bioinformatics Core at National Cancer Institute for help with genomics and miRNA data analysis. We also thank Charlotte Hanson and Michael Sanford for help with technical assistance. This research was supported by the Intramural Research Program of the NIH, Center for Cancer Research, National Cancer Institute. The authors declare no competing financial interests.

Appendix A. Supplementary data

Supplementary data to this article can be found online at https://doi.org/10.1016/j.jaut.2020.102436.

Financial support

This work has been funded with federal funds from the National Cancer Institute Intramural Program Funding BC009283, National Institutes of Health, United States to HAY; University of California Davis School of Medicine, United States NIH award DK123262 to MEG.

References

[1] P. Hunter, The inflammation theory of disease. The growing realization that chronic inflammation is crucial in many diseases opens new avenues for treatment, EMBO Rep. 13 (2012) 968–970.
[2] C.H. Liu, N.D. Abrams, D.M. Carrick, P. Chander, J. Dwyer, M.R.J. Hamlet, et al., Biomarkers of chronic inflammation in disease development and prevention: challenges and opportunities, Nat. Immunol. 18 (2017) 1175–1180.
[3] A.M. Ercolini, S.D. Miller, The role of infections in autoimmune disease, Clin. Exp. Immunol. 155 (2009) 1–15.
[4] C.E. Samuel, Antiviral actions of interferons, Clin. Microbiol. Rev. 14 (2001) 778–809 table of contents.
[5] O. Meyer, Interferons and autoimmune disorders, Joint Bone Spine : revue du rhumatisme 76 (2009) 464–473.
[6] J.C. Hall, L. Casciola-Rosen, A.E. Berger, E.K. Kapsogeorgou, C. Cheadle, A.G. Tzioufas, et al., Precise probes of type II interferon activity define the origin of interferon signatures in target tissues in rheumatic diseases, Proc. Natl. Acad. Sci. U.S.A. 109 (2012) 17609–17614.
[7] D.L. Hodge, C. Berthet, V. Coppola, W. Kastenmuller, M.D. Buschman, P.M. Schaughency, et al., IFN-gamma AU-rich element removal promotes chronic IFN-gamma expression and autoimmunity in mice, J. Autoimmun. 53 (2014) 33–45.
[8] H.R. Bae, P.S. Leung, K. Tsuneyama, J.C. Valencia, D.L. Hodge, S. Kim, et al., Chronic expression of interferon-gamma leads to murine autoimmune cholangitis with a female predominance, Hepatology 64 (2016) 1189–1201.
[9] H.R. Bae, D.L. Hodge, G.X. Yang, P.S.C. Leung, S.B. Chodisetti, J.C. Valencia, et al., The interplay of type I and type II interferons in murine autoimmune cholangitis as a basis for sex-biased autoimmunity, Hepatology 67 (2018) 1408–1419.
[10] S.T. Ngo, F.J. Steyn, P.A. McCombe, Gender differences in autoimmune disease, Front. Neuroendocrinol. 35 (2014) 347–369.
[11] E. Cirillo, L.D. Parnell, C.T. Evelo, A review of pathway-based analysis tools that visualize genetic variants, Front. Genet. 8 (2017) 174.
[12] R.A. Miller, F. Ehrhart, L.M.T. Eijssen, D.N. Slenter, L.M.G. Curfs, C.T. Evelo, et al., Beyond pathway analysis: identification of active subnetworks in rett syndrome, Front. Genet. 10 (2019) 59.
[13] C.A. Piccirillo, E. Bjur, I. Topisirovic, N. Sonenberg, O. Larsson, Translational control of immune responses: from transcripts to translatomes, Nat. Immunol. 15 (2014) 503–511.
[14] Modifying immunity, Nat. Immunol. 15 (2014) 483.
[15] J.G. Caporaso, J. Kuczynski, J. Stombaugh, K. Bittinger, F.D. Bushman, E.K. Costello, et al., QIIME allows analysis of high-throughput community sequencing data, Nat. Methods 7 (2010) 335–336.
[16] B.J. Callahan, P.J. McMurdie, M.J. Rosen, A.W. Han, A.J. Johnson, S.P. Holmes, DADA2: high-resolution sample inference from Illumina amplicon data, Nat. Methods 13 (2016) 581–583.
[17] C. Quast, E. Pruesse, P. Yilmaz, J. Gerken, T. Schweer, P. Yarza, et al., The SILVA ribosomal RNA gene database project: improved data processing and web-based tools, Nucleic Acids Res. 41 (2013) D590–D596.
[18] A.M. Evans, C.D. DeHaven, T. Barrett, M. Mitchell, E. Milgram, Integrated, nontargeted ultrahigh performance liquid chromatography/electrospray ionization tandem mass spectrometry platform for the identification and relative quantification of the small-molecule complement of biological systems, Anal. Chem. 81 (2009) 6656–6667.
[19] G. Sharon, N. Garg, J. Debelius, R. Knight, P.C. Dorrestein, S.K. Mazmanian, Specialized metabolites from the microbiome in health and disease, Cell Metabol. 20 (2014) 719–730.
[20] L.S. Zhang, S.S. Davies, Microbial metabolism of dietary components to bioactive metabolites: opportunities for new therapeutic interventions, Genome Med. 8 (2016) 46.
[21] T. Yamano, J. Nedjic, M. Hinterberger, M. Steinert, S. Koser, S. Pinto, et al., Thymic B cells are licensed to present self antigens for central T cell tolerance induction, Immunity 42 (2015) 1048–1061.
[22] A. Hevia, C. Milani, P. Lopez, A. Cuervo, S. Arboleya, S. Duranti, et al., Intestinal dysbiosis associated with systemic lupus erythematosus, mBio 5 (2014) e01548-14.
[23] T. Mandl, J. Marsal, P. Olsson, B. Ohlsson, K. Andreasson, Severe intestinal dysbiosis is prevalent in primary Sjogren's syndrome and is associated with systemic disease activity, Arthritis Res. Ther. 19 (2017) 237.
[24] R. Tang, Y. Wei, Y. Li, W. Chen, H. Chen, Q. Wang, et al., Gut microbial profile is altered in primary biliary cholangitis and partially restored after UDCA therapy, Gut 67 (2018) 534–541.
[25] J. Chen, N. Chia, K.R. Kalari, J.Z. Yao, M. Novotna, M.M. Paz Soldan, et al., Multiple sclerosis patients have a distinct gut microbiota compared to healthy controls, Sci. Rep. 6 (2016) 28484.
[26] X.M. Luo, M.R. Edwards, Q. Mu, Y. Yu, M.D. Vieson, C.M. Reilly, et al., Gut microbiota in human systemic lupus erythematosus and a mouse model of lupus, Appl. Environ. Microbiol. (2018) 84.
[27] W. Chen, Y. Wei, A. Xiong, Y. Li, H. Guan, Q. Wang, et al., Comprehensive analysis of serum and fecal bile acid profiles and interaction with gut microbiota in primary biliary cholangitis, Clin. Rev. Allergy Immunol. 58 (1) (2020) 25–38.
[28] K.S. Ost, J.L. Round, A Few Good Commensals, Gut microbes use IFN-gamma to fight Salmonella, Immunity 46 (2017) 977–979.
[29] S. Della Torre, N. Mitro, C. Meda, F. Lolli, S. Pedretti, M. Barcella, et al., Short-term fasting reveals amino acid metabolism as a major sex-discriminating factor in the liver, Cell Metabol. 28 (2018) 256–267 e5.
[30] M. Grabacka, M. Pierzchalska, M. Dean, K. Reiss, Regulation of ketone body metabolism and the role of PPARalpha, Int. J. Mol. Sci. 17 (2016).
[31] M. Wajner, A.U. Amaral, Mitochondrial dysfunction in fatty acid oxidation disorders: insights from human and animal studies, Biosci. Rep. 36 (2015) e00281.
[32] S.M. Houten, R.J. Wanders, A general introduction to the biochemistry of mitochondrial fatty acid beta-oxidation, J. Inherit. Metab. Dis. 33 (2010) 469–477.
[33] M. Makrecka-Kuka, E. Sevostjanovs, K. Vilks, K. Volska, U. Antone, J. Kuka, et al., Plasma acylcarnitine concentrations reflect the acylcarnitine profile in cardiac tissues, Sci. Rep. 7 (2017) 17528.
[34] M.I. Malandrino, R. Fucho, M. Weber, M. Calderon-Dominguez, J.F. Mir, L. Valcarcel, et al., Enhanced fatty acid oxidation in adipocytes and macrophages reduces lipid-induced triglyceride accumulation and inflammation, Am. J. Physiol. Endocrinol. Metabol. 308 (2015) E756–E769.
[35] D. Namgaladze, B. Brune, Macrophage fatty acid oxidation and its roles in macrophage polarization and fatty acid-induced inflammation, Biochim. Biophys. Acta 1861 (2016) 1796–1807.
[36] W.A. Alaynick, Nuclear receptors, mitochondria and lipid metabolism, Mitochondrion 8 (2008) 329–337.
[37] S.I. Sayin, A. Wahlstrom, J. Felin, S. Jantti, H.U. Marschall, K. Bamberg, et al., Gut microbiota regulates bile acid metabolism by reducing the levels of tauro-beta-muricholic acid, a naturally occurring FXR antagonist, Cell Metabol. 17 (2013) 225–235.
[38] B.S. Wostmann, Intestinal bile acids and cholesterol absorption in the germfree rat, J. Nutr. 103 (1973) 982–990.
[39] A. Wahlstrom, Outside the liver box: the gut microbiota as pivotal modulator of liver diseases, Biochim. Biophys. Acta (BBA) - Mol. Basis Dis. 1865 (2019) 912–919.
[40] A. Wahlstrom, S.I. Sayin, H.U. Marschall, F. Backhed, Intestinal crosstalk between bile acids and microbiota and its impact on host metabolism, Cell Metabol. 24 (2016) 41–50.
[41] J. Gao, K. Xu, H. Liu, G. Liu, M. Bai, C. Peng, et al., Impact of the gut microbiota on intestinal immunity mediated by tryptophan metabolism, Frontiers in cellular and infection microbiology 8 (2018) 13.
[42] B. Lamas, J.M. Natividad, H. Sokol, Aryl hydrocarbon receptor and intestinal immunity, Mucosal Immunol. 11 (2018) 1024–1038.
[43] R. Shinde, T.L. McGaha, The aryl hydrocarbon receptor: connecting immunity to the microenvironment, Trends Immunol. 39 (2018) 1005–1020.
[44] S. Crunkhorn, Autoimmune disease: aryl hydrocarbon receptor suppresses inflammation, Nat. Rev. Drug Discov. 17 (2018) 470.
[45] N. Hao, M.L. Whitelaw, The emerging roles of AhR in physiology and immunity, Biochem. Pharmacol. 86 (2013) 561–570.
[46] L.M. Wang, Y. Zhang, X. Li, M.L. Zhang, L. Zhu, G.X. Zhang, et al., Nr4a1 plays a crucial modulatory role in Th1/Th17 cell responses and CNS autoimmunity, Brain Behav. Immun. 68 (2018) 44–55.
[47] D.S. Koenis, L. Medzikovic, P.B. van Loenen, M. van Weeghel, S. Huveneers, M. Vos, et al., Nuclear receptor Nur77 limits the macrophage inflammatory response through transcriptional reprogramming of mitochondrial metabolism, Cell Rep. 24

(2018) 2127–21240 e7.
[48] G.M. Tannahill, A.M. Curtis, J. Adamik, E.M. Palsson-McDermott, A.F. McGettrick, G. Goel, et al., Succinate is an inflammatory signal that induces IL-1beta through HIF-1alpha, Nature 496 (2013) 238–242.
[49] C. Serena, V. Ceperuelo-Mallafre, N. Keiran, M.I. Queipo-Ortuno, R. Bernal, R. Gomez-Huelgas, et al., Elevated circulating levels of succinate in human obesity are linked to specific gut microbiota, ISME J. 12 (2018) 1642–1657.
[50] S. Perez-Sieira, G. Martinez, B. Porteiro, M. Lopez, A. Vidal, R. Nogueiras, et al., Female Nur77-deficient mice show increased susceptibility to diet-induced obesity, PloS One 8 (2013) e53836.
[51] H.J. Park, J.M. Choi, Sex-specific regulation of immune responses by PPARs, Exp. Mol. Med. 49 (2017) e364.
[52] H.J. Park, H.S. Park, J.U. Lee, A.L. Bothwell, J.M. Choi, Gender-specific differences in PPARgamma regulation of follicular helper T cell responses with estrogen, Sci. Rep. 6 (2016) 28495.
[53] K.J. Waite, Z.E. Floyd, P. Arbour-Reily, J.M. Stephens, Interferon-gamma-induced regulation of peroxisome proliferator-activated receptor gamma and STATs in adipocytes, J. Biol. Chem. 276 (2001) 7062–7068.
[54] M. Pascual-Garcia, L. Rue, T. Leon, J. Julve, J.M. Carbo, J. Matalonga, et al., Reciprocal negative cross-talk between liver X receptors (LXRs) and STAT1: effects on IFN-gamma-induced inflammatory responses and LXR-dependent gene expression, J. Immunol. 190 (2013) 6520–6532.
[55] B. Renga, M. Migliorati, A. Mencarelli, S. Fiorucci, Reciprocal regulation of the bile acid-activated receptor FXR and the interferon-gamma-STAT-1 pathway in macrophages, Biochim. Biophys. Acta 1792 (2009) 564–573.
[56] V. Klepsch, A.R. Moschen, H. Tilg, G. Baier, N. Hermann-Kleiter, Nuclear receptors regulate intestinal inflammation in the context of IBD, Front. Immunol. 10 (2019) 1070.
[57] E. Garcia-Gomez, B. Gonzalez-Pedrajo, I. Camacho-Arroyo, Role of sex steroid hormones in bacterial-host interactions, BioMed Res. Int. 2013 (2013) 928290.
[58] Y. You, R.C. Myers, L. Freeberg, J. Foote, J.F. Kearney, L.B. Justement, et al., Marginal zone B cells regulate antigen capture by marginal zone macrophages, J. Immunol. 186 (2011) 2172–2181.
[59] N. Nikbakht, S. Shen, T. Manser, Cutting edge: macrophages are required for localization of antigen-activated B cells to the follicular perimeter and the subsequent germinal center response, J. Immunol. 190 (2013) 4923–4927.
[60] C. Kelly, C. Jefferies, S.A. Cryan, Targeted liposomal drug delivery to monocytes and macrophages, Journal of drug delivery 2011 (2011) 727241.
[61] N. van Rooijen, A. Sanders, T.K. van den Berg, Apoptosis of macrophages induced by liposome-mediated intracellular delivery of clodronate and propamidine, J. Immunol. Methods 193 (1996) 93–99.
[62] D.L. Bonilla, A. Bhattacharya, Y. Sha, Y. Xu, Q. Xiang, A. Kan, et al., Autophagy regulates phagocytosis by modulating the expression of scavenger receptors, Immunity 39 (2013) 537–547.
[63] E.A. Oczypok, T.D. Oury, C.T. Chu, It's a cell-eat-cell world: autophagy and phagocytosis, Am. J. Pathol. 182 (2013) 612–622.
[64] V.L. Crotzer, J.S. Blum, Autophagy and its role in MHC-mediated antigen presentation, J. Immunol. 182 (2009) 3335–3341.
[65] R.T. Netea-Maier, T.S. Plantinga, F.L. van de Veerdonk, J.W. Smit, M.G. Netea, Modulation of inflammation by autophagy: consequences for human disease, Autophagy 12 (2016) 245–260.
[66] M. Pierdominici, M. Vomero, C. Barbati, T. Colasanti, A. Maselli, D. Vacirca, et al., Role of autophagy in immunity and autoimmunity, with a special focus on systemic lupus erythematosus, Faseb. J. : official publication of the Federation of American Societies for Experimental Biology 26 (2012) 1400–1412.
[67] D.J. Wu, I.E. Adamopoulos, Autophagy and autoimmunity, Clin. Immunol. 176 (2017) 55–62.
[68] L.A. Baxt, R.J. Xavier, Role of autophagy in the maintenance of intestinal homeostasis, Gastroenterology 149 (2015) 553–562.
[69] L. Yang, C. Liu, W. Zhao, C. He, J. Ding, R. Dai, et al., Impaired autophagy in intestinal epithelial cells alters gut microbiota and host immune responses, Appl. Environ. Microbiol. (2018) 84.
[70] A.L. DeFranco, Germinal centers and autoimmune disease in humans and mice, Immunol. Cell Biol. 94 (2016) 918–924.
[71] V. Deretic, B. Levine, Autophagy balances inflammation in innate immunity, Autophagy 14 (2018) 243–251.
[72] T. Prabakaran, C. Bodda, C. Krapp, B.C. Zhang, M.H. Christensen, C. Sun, et al., Attenuation of cGAS-STING signaling is mediated by a p62/SQSTM1-dependent autophagy pathway activated by TBK1, EMBO J. 37 (2018).
[73] Y. Kato, J. Park, H. Takamatsu, H. Konaka, W. Aoki, S. Aburaya, et al., Apoptosis-derived membrane vesicles drive the cGAS-STING pathway and enhance type I IFN production in systemic lupus erythematosus, Ann. Rheum. Dis. 77 (2018) 1507–1515.
[74] J.M. Lee, M. Wagner, R. Xiao, K.H. Kim, D. Feng, M.A. Lazar, et al., Nutrient-sensing nuclear receptors coordinate autophagy, Nature 516 (2014) 112–115.
[75] G.A. Preidis, K.H. Kim, D.D. Moore, Nutrient-sensing nuclear receptors PPARalpha and FXR control liver energy balance, J. Clin. Invest. 127 (2017) 1193–1201.
[76] A. Remmerie, C.L. Scott, Macrophages and lipid metabolism, Cell. Immunol. 330 (2018) 27–42.